https://doi.org/10.5194/egusphere-2025-634
Preprint. Discussion started: 21 February 2025

Assessing the sensitivity of storm surge simulation to the atmospheric forcing resolutions across the estuary-sea continuum

Ny Riana Randresihaja[1,2], Olivier Gourgue[3], Lauranne Alaerts[1,2], Xavier Fettweis[5], Jonathan Lambrechts[4], Miguel De Le Court[4], Marilaure Grégoire[2], and Emmanuel Hanert[1,4]

[1]Earth and Life Institute (ELI), UCLouvain, Louvain-la-Neuve, Belgium
[2]Department of Astrophysics, Geophysics and Oceanography (AGO), ULiège, Liège, Belgium
[3]Operational Directorate Natural Environment (OD Nature), Royal Belgian Institute of Natural Sciences (RBINS), Brussels, Belgium
[4]Institute of Mechanics, Materials and Civil Engineering (IMMC), UCLouvain, Louvain-la-Neuve, Belgium
[5]SPHERES research units, Geography Department, ULiège, Liège, Belgium

Correspondence: Ny Riana Randresihaja (ny.randresihaja@uclouvain.be)

Abstract. Estuaries are particularly vulnerable to flooding from extreme events such as storm surges, and this vulnerability can be exacerbated by climate change. Numerical models are valuable tools for supporting flood prevention and planning in these regions. However, despite recent improvements in storm surge modeling, most models use atmospheric forcing data with spatial resolutions of several tens of kilometers and temporal resolutions of a few hours, hence much coarser than their own resolution. This discrepancy may have an impact on the overall model accuracy. Here, we evaluate the impact of atmospheric forcing data's spatial and temporal resolution on storm surge modeling within the Scheldt river-estuary-North Sea sea continuum. Atmospheric forcings were incorporated at spatial resolutions ranging from 2 km to 30 km and at temporal resolutions from 15 minutes to 6 hours. Using an unstructured-mesh multiscale hydrodynamic model, we assessed how these variations influenced the accuracy of storm surge simulations. Our findings indicate that increasing spatial resolution significantly improves the accuracy of peak surge predictions in estuarine areas, while higher temporal resolution further enhances model performance only at the finest spatial resolution. The effect of the temporal resolution diminishes as spatial resolution becomes coarser, suggesting that spatial resolution is more critical for improving storm surge forecasts in estuaries like the Scheldt. The timing of peak surges remained consistent across all configurations. The best results are obtained with 2 km and 15 min atmospheric forcing resolution. This study underscores the importance of aligning atmospheric forcing resolution with the hydrodynamic model's spatial scale to achieve optimal accuracy in storm surge predictions for estuaries.

1 Introduction

Storm surges pose significant risks to human safety, particularly given that nearly 15% of the global population lives in coastal areas (Cosby et al., 2024). An estimated 1.3% of the world's population is exposed to 1-in-100-year flood events, which have the potential to cause economic damages reaching up to 11 trillion USD (Nicholls, 2006; Bouwer, 2011). The consequences of such events are severe infrastructure damage, essential services disruption, and threats on natural habitats, resulting in substantial socioeconomic impacts. The risks are even more pronounced in densely populated areas such as estuaries where the funnel-

https://doi.org/10.5194/egusphere-2025-634
Preprint. Discussion started: 21 February 2025

shaped topography can further amplify the surge. As key transitional zones in the land-sea continuum, estuaries are particularly vulnerable to storm surges due to the combined effects of river discharge and offshore hydrometeorological conditions (Ward et al., 2020). Consequences of storm surge in estuaries include intensified saltwater intrusion, which disrupts stratification and biogeochemical processes (Statham, 2012; Wetz and Yoskowitz, 2013). The risk on these regions is further heightened when storm surges coincide with significant rainfall or high river discharge, leading to exacerbated flooding (Marcos et al., 2019). Accurately modeling storm surges in these areas is essential for developing effective mitigation strategies and informing policy decisions.

Simulating processes along estuaries-sea continuum is a challenging task. This is due to the broad range of spatial and temporal scales involved, from tens of meters within estuaries to hundreds of kilometers across coastal regions and continental shelves (Marchesiello et al., 2001; Lewis et al., 2019). Historically, these scale discrepancies have led to under-representation of estuaries in coastal models, while estuarine hydrodynamic models often lack the scope to extend over adjacent coastal regions (Marchesiello et al., 2001). However, advances in modeling techniques, powered by improved computational capabilities, innovative algorithms, and enhanced data integration and assimilation, have significantly bridged this gap (Shu et al., 2011; Kärnä et al., 2011; Le et al., 2020; Verri et al., 2023). These integrated land-sea models are now applied not only to resolve physical processes but also to explore bio-geochemical interactions, deepening our understanding of the river-ocean continuum (de Brye et al., 2010; Kärnä et al., 2011; Rodrigues et al., 2015; Vallaeys et al., 2021). This progress has proven especially valuable in storm surge modeling in land-sea continuum, where it has enhanced insights into models sensitivity to varying parametrization and highlighted the primary forcing mechanisms during such events (Garzon and Ferreira, 2016; Yang et al., 2020).

Despite these advances, certain aspects of the land-sea continuum modeling remain poorly understood. One unresolved aspect is how atmospheric forcing resolution influences storm surge prediction. Although atmospheric conditions are the primary drivers of storm surge dynamics, the finer resolution of estuarine-sea models is generally not matched by the spatial resolution of the atmospheric forcing, with the latter typically operating on scales of tens of kilometers (Dinápoli et al., 2020; Chen et al., 2023). Small-scale processes such as localized wind patterns, frontal systems, and pressure gradients are smoothed out in coarse-resolution atmospheric data. As a result, these unresolved processes within estuaries can introduce errors in the simulated surge dynamics, impacting factors like the timing, peak intensity, and spatial distribution.

In the context of the Scheldt estuary-sea continuum, existing models of the river system tend to simplify or exclude the influence of North Sea conditions on estuarine dynamics. While some exceptions extend two-dimensional (2D) models of the Scheldt into nearby coastal regions of the North Sea, these focus largely on eco-hydrodynamics (Vanderborght et al., 2007; de Brye et al., 2010; Arndt et al., 2011). Other studies have modeled the land-sea continuum under storm surge conditions, but they have mostly focused on the mitigating effects of retention areas (Smolders et al., 2015). No existing research has specifically examined how variations in atmospheric forcing resolution impact storm surge behavior across this continuum.

The North Sea, situated within the Northwestern European Continental Shelf (NWCS), and connected with the Scheldt river (Fig. 1), is highly vulnerable to storm surges. The region's shallow bathymetry amplifies water level rise during surge events, especially along the southern North Sea coastlines of Belgium, the Netherlands, and Germany (Sündermann and Pohlmann, 2011). Major storm surge events occurred in 1963 and 2013, the former of which have prompted the authorities to strengthen coastal surge barriers along the southern coastline. Under climate change, those event are expected to increase in intensity (Woth et al., 2006). Previous studies have explored how different atmospheric forcing models affect storm surge simulation across the NWCS during those surge events, with findings highlighting the importance of high spatio-temporal resolution in capturing surge magnitude and duration accurately (Muller et al., 2014; Ridder et al., 2018; Agulles et al., 2024; Meyer and Gaslikova, 2023). However, those studies mainly focused on coastal region and have largely neglected the specific complexities of estuarine dynamics.

In this study, we assess the impact of spatial and temporal resolution of atmospheric forcing on storm surge simulation within the Scheldt land-sea continuum. We couple a high-resolution, multiscale coastal ocean model with a high-resolution atmospheric model to explore how atmospheric forcing resolution affects the accuracy of ocean model outputs during a storm event in the Scheldt estuary and North Sea. Our analysis begins by assessing the model's capability to capture regional dynamics by employing high-resolution atmospheric inputs, specifically focusing on the extra-tropical storm Xaver, which significantly affected the area of interest on December 5-6, 2013 (Fig. 2.a). Model performances are assessed by comparing the simulations with in-situ data. Then, we evaluate the sensitivity of storm surge simulations to variations in the atmospheric model resolution, examining both spatial granularity and temporal frequency in the estuarine region.

2 Materials and methods

2.1 Study area

The Scheldt estuary spans through Belgium and the Netherlands and flows north along the Northwestern European Continental Shelf (NWCS) in the North Sea (Fig. 1). Upstream, the tidal signal extends up to 160 km from the river mouth. River discharge from the Scheldt and its tributaries is negligible compared to the tidal volume, resulting in a well-mixed estuary with minimal vertical salinity gradients (Meire et al., 2005; Van Damme et al., 2005). The funnel-shaped morphology of the estuary enhances tidal amplitudes that reach a tidal range of 6 m near Antwerp. As a result of the large tidal variation, the Scheldt estuary features intertidal flats and marshes that periodically flood and dry out. Human interventions, such as embankment construction and dredging, have modified the estuary over time, increasing tidal ranges, and altering storm surge dynamics. Other modifications include large flood control areas to improve safety and create new intertidal habitats (Schepers et al., 2018). Nowadays, the estuary has two deep channels separated by shoals and bordered by tidal flats, as indicated by the negative bathymetry region in the lower estuary (Fig. 1.a). Downstream, the Scheldt meets the North Sea, which connects to the Atlantic Ocean via the northern boundary and the English Channel to the south (Fig. 2.a). The regional dynamics of the North Sea is shaped by oceanic and atmospheric factors such as tides and the North Atlantic Oscillation (NAO), as well as continental influences, including river discharges and pollutant and nutrient inputs from major rivers such as the Thames, Seine, Meuse-Rhine, and Scheldt (Sündermann and Pohlmann, 2011; Ivanov et al., 2020).

The NWCS experiences storm surges during autumn and winter, driven by extratropical cyclones that follow the North Atlantic storm track (Nicholls, 2006; Resio and Westerink, 2008). These cyclones, often originating from the polar front, cause

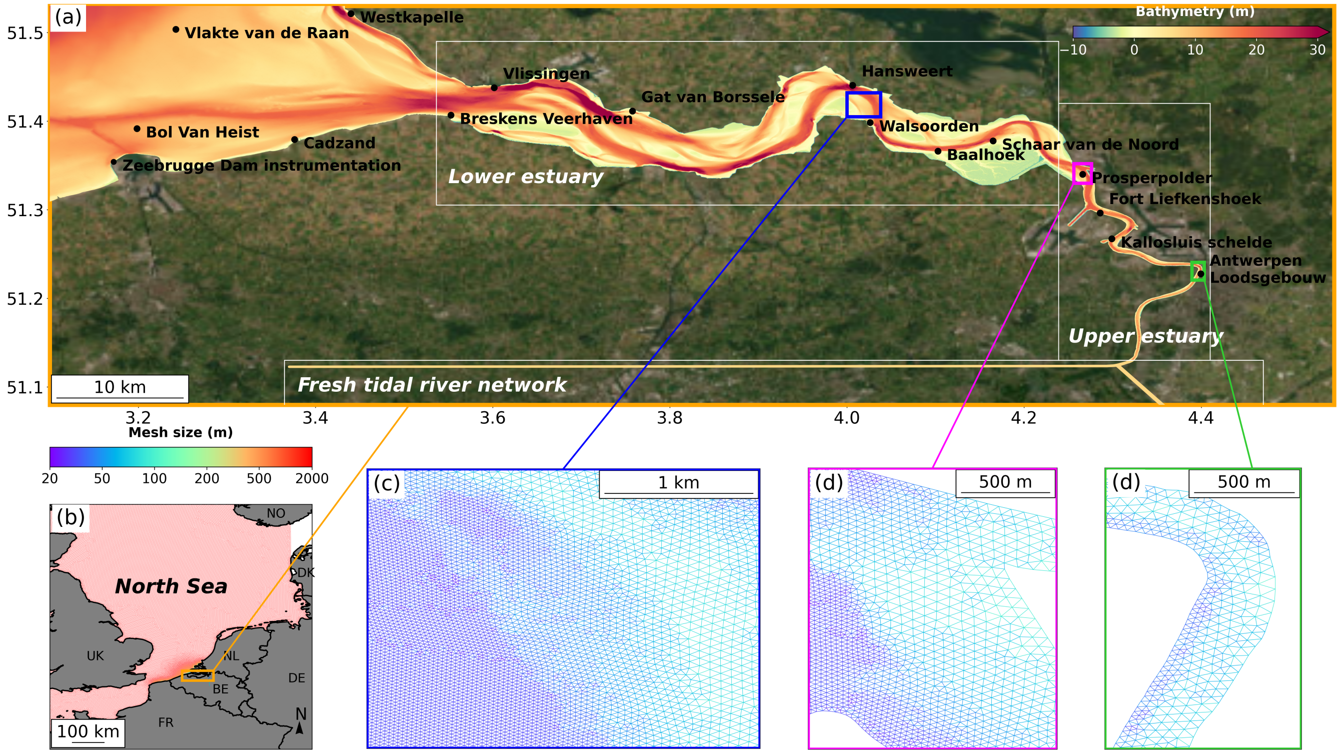

Figure 1. Model computation domain covering the Scheldt and North Sea region. The upper panel (a) displays the bathymetry of the Scheldt estuary, where black dots mark validation points for the hydrodynamic model with Esri World Imagery as basemap (ESRI, 2025). The white rectangles outline the tidal zones of the estuary and the fresh tidal river network is represented by artificial linear channels. Lower panels show the unstructured mesh configuration with (b) large view across the North Sea and (c-e) close-up views at three distinct locations on the Scheldt estuary.

localized sea level rises, positive surges, due to drops in atmospheric pressure and wind stress (Bierly, 2005). Although atmospheric pressure deficits are the main driver of storm surges in deeper waters, wind stress becomes increasingly significant near the coast, causing water to accumulate and resulting in surges of up to 4 m along coastal North Sea (Mathers and Woodworth, 2004; Weisse et al., 2012; Dangendorf et al., 2014). The intensity and direction of the surge are also shaped by regional factors, such as bathymetry and the configuration of the coastline, and can be amplified by astronomical tides (Pugh, 1987; Kerr et al., 2013; Marcos et al., 2019). Here we model the effect of the extra-tropical storm event Xaver that impacted the North Sea and its surroundings on December 5-6, 2013. It formed in Greenland and grew while traveling North of Scotland up to the Baltic Sea (Fig. 2.a). This historic event was a superposition of a spring tide and a storm surge due to strong northwesterly winds over the North Sea, resulting in surge levels surpassing the typical tidal signal by more than 4 m at several locations along the eastern North Sea coast and 2.5 m at Antwerp (Flikweert et al., 2016).

2.2 The circulation model

In this study, we use the multiscale ocean model SLIM (Second-generation Louvain-la-Neuve Ice-ocean Model) to simulate the hydrodynamics of the Scheldt estuary and North Sea continuum. This model is specifically designed to address multiscale processes in coastal ocean region with complex topography and bathymetry. SLIM has already been applied to the Scheldt river and estuary and its coastal area (de Brye et al., 2010; de Brauwere et al., 2011; Kärnä et al., 2011; Gourgue et al., 2013; Patil et al., 2024). The model has also been successfully applied to various riverine systems worldwide, including the Mahakam and Kapuas river deltas in Indonesia (Sampurno et al., 2022; Draoui et al., 2024) and the Columbia river in the US (Vallaeys et al., 2018, 2021). Since then, the model has evolved and recent updates allow running simulations on GPUs which considerably reduced the computation time.

We consider the 2D depth-integrated version of SLIM (Lambrechts et al., 2008), which is suited for regions like the Scheldt estuary characterized by small depth and predominantly well-mixed conditions (Meire et al., 2005; Van Damme et al., 2005). The model solves the shallow water equations for the sea surface elevation η and depth-integrated velocity $\mathbf{u}$ using the Discontinuous Galerkin (DG) finite element method over an unstructured mesh. These equations are expressed as follows:

$$\frac{\partial \eta}{\partial t} + \nabla_h \cdot (H\mathbf{u}) = 0, \tag{1}$$

$$\frac{\partial (H\mathbf{u})}{\partial t} + \nabla_h \cdot \frac{H\mathbf{u}H\mathbf{u}}{H} = -f\mathbf{e}_z \times H\mathbf{u} - gH\nabla_h \eta - \frac{g}{(\gamma H)^2}|H\mathbf{u}|H\mathbf{u} + \nabla_h \cdot H\nu_h \nabla_h \mathbf{u} + \frac{\boldsymbol{\tau}_s}{\rho} - \frac{H}{\rho}\nabla_h p_{\text{atm}}, \tag{2}$$

where t is time, ∇_h is the horizontal gradient operator, and the water column height is $H = d + \eta$, with d as the water depth below the reference level. The Coriolis factor is given by $f = 2\Omega \sin\Phi$,where Ω is the Earth's angular velocity and Φ is the latitude , $\mathbf{e}_z$ is a vertical unit vector, g is the gravitational acceleration, γ is the bottom stress, ν_h is the horizontal eddy viscosity, $\boldsymbol{\tau}_s = (\tau_x, \tau_y)$ is the wind surface stress and ρ is the water density. The model initial conditions are $\mathbf{u} = (0,0)$ m/s and $\eta = 0$ m.

The bottom stress is parametrized as a quadratic expression, where the Chezy-Manning-Strickler bottom-stress coefficient is $\gamma = \frac{H^{1/6}}{n}$, with n being the Manning coefficient. In coastal and estuarine modeling, typical Manning values fall within the range of 0.02 to 0.2 s $\mathrm{m}^{-1/3}$ (Kjerfve et al., 1991). A map of the Manning area is described in Appendix B. We use in the coastal regions of the North Sea a Manning coefficient of $0.025\,\mathrm{s\,m}^{-1/3}$, while offshore regions were set with a constant coefficient of $0.02\,\mathrm{s\,m}^{-1/3}$. For the upstream portion of the estuary, a larger coefficient of $0.04\,\mathrm{s\,m}^{-1/3}$ is used (Kolokythas, G. et al., 2021). In the lower estuary, a junction of riverine and maritime influences, we used a Manning coefficient of $0.012\,\mathrm{s\,m}^{-1/3}$. Vegetation-rich tidal marshes and flats were assigned a coefficient of $0.08\,\mathrm{s\,m}^{-1/3}$ based on vegetation friction estimates (Wamsley et al., 2010; Stark et al., 2017). Though vegetation is represented through bottom friction, this approach has limitations, as it underestimates friction when water depths are below vegetation height. This limitation was deemed acceptable in our study, as high water levels during storm surges are expected to fully submerge the vegetation. The effects of unresolved turbulent motions is considered through the Smagorinsky (1963) parametrization of the horizontal eddy viscosity.

Finally, the last parametrization concerns the wind stress $\boldsymbol{\tau}_s$, which depends on the wind as external forcing, with $\mathbf{u}_{10}$ being the wind speed at 10 m above the sea surface:

$$\boldsymbol{\tau}_s = \rho_{\text{air}} C_w ||\mathbf{u}_{10}||\mathbf{u}_{10},$$

where $\rho_{\text{air}} = 1.25\,\mathrm{kg\,m}^{-3}$ is the air density and C_w is the wind drag coefficient. The wind speed is retrieved from the regional atmospheric model MAR, described in Section 2.3.3. To account for the increased roughness of the sea surface caused by strong winds, the drag coefficient is parameterized as a function of wind speed. The value of C_w saturates for high wind speed, specially relevant in the context of a storm surge. This saturation occurs due to the spume effect, where intense winds produce large volumes of sea spray by tearing water droplets from wave crests (Powell et al., 2003; Donelan et al., 2004; Holthuijsen et al., 2012; Curcic and Haus, 2020). We take this saturation effect into account by using the wind drag parameterization of Flather (1976):

$$C_w = \begin{cases} 0.565 \cdot 10^{-3} & \text{if } \|\mathbf{u}_{10}\| \leq 5 \text{ m/s}, \\ (-0.12 + 0.137\|\mathbf{u}_{10}\|) \cdot 10^{-3} & \text{if } 5 \leq \|\mathbf{u}_{10}\| \leq 19.22 \text{ m/s}, \\ 2.513 \cdot 10^{-3} & \text{if } \|\mathbf{u}_{10}\| \geq 19.22 \text{ m/s}. \end{cases}$$

The North Sea and Scheldt estuary region experience pronounced tidal amplitudes, with water level fluctuations reaching up to 6 m between high and low tides. These fluctuations result in periodic wetting and drying (WD) of certain shallow estuarine areas, a phenomenon further exacerbated during storm surges. When areas of the estuary become dry, numerical complications can arise as the $H \to 0$ in Eq. (2). The current version of SLIM uses an explicit WD algorithm, which can increase the computational cost, especially for large-scale simulations. More details on the WD scheme are provided in Appendix C.

2.3 Model set up

A one-month simulation was conducted from November 20 to December 20, 2013, with a five-day spin-up phase excluded from validation to eliminate transient effects from the model's initial conditions. Our study focuses on the estuarine region of the Scheldt, incl. the upper estuary, the lower estuary, the river mouth, and its direct coastal surroundings (Fig. 1.a). The freshwater tidal river is modeled as a simplified, straight channel (Fig. 1.a), following the approach of Bart De Maerschalck et al. (2023). This approach enables the representation of tidal signal attenuation as tides propagates upstream the estuary. The model set up spans from the upper Scheldt estuary with a minimum resolution of 20 m (Fig. 1.a) to the 200 m isobath, where the resolution transitions to 2 km in the North Sea (Fig. 1.b). Setting the domain up to the continental shelf provides more coherent boundary conditions, better integration of river discharges and improves wind-driven simulations such as storm surges (de Brye et al., 2010).

The unstructured mesh is generated using the seamsh Python library, which is based on the open-source mesh generator software GMSH (Geuzaine and Remacle, 2009) and comprises approximately 2×10^6 triangles. The mesh discretization of the estuary follows the course of the Scheldt river, from its mouth to the beginning of the freshwater tidal river network with a mesh resolution adapted according to the bathymetry (Fig. 1.c-e), with a finer resolution reaching 20 m in shallower areas and around 50 m near the river centerline. Simulations were run on four Nvidia A100 GPUs. A one month simulation took about two hours of computing time for the mesh described above. A preliminary calibration of the Manning coefficient along the domain during calm weather was also performed, but as this study focuses on the Storm Xaver period, it is detailed separately in Appendix B.

2.3.1 Bathymetry

We use multiple data sources to characterize the bathymetry across our computational domain, selecting them based on the finest resolution available over the region. Starting with a coarser resolution over the NWCS, the bathymetry becomes finer as we approach the Scheldt estuary, reaching a mimimum resolution of 10 m within the estuary. The data sources are presented in the upper part of Table 1. Over the NWCS, we use bathymetry data from the EMODnet (2021) dataset, which has a resolution of 115 m. Closer to the Dutch coast and into the lower Scheldt estuary, we use higher-resolution data from Rijkwaterstaat (2021) at a resolution of 100 m. As we move further towards the upper Scheldt estuary, we refine the bathymetry using data from AGENTSCHAP MDK (2021), which provides a 10 m resolution for the shallowest regions of the estuary. We then combine and convert these datasets to the same datum, NAP, to ensure consistency across the entire domain. The reference level NAP is used in the Netherlands and is generally equivalent to the mean sea level (MSL) from sources like EMODNet. However, there is a 2.33 m difference between NAP and the Belgian reference level Tweede Algemene Waterpassing (TAW), with TAW being lower. In the schematized freshwater tidal river a constant bathymetry of 7 m is provided, reflecting the mean bathymetry in this part of the river. A map describing the data sources and their locations in the domain is available in Appendix A.

2.3.2 Oceanic and continental forcings

We impose tides and residual currents at the open lateral boundaries of the domain on the continental shelf. The tidal dynamics in the region are taken into account by applying a tidal forcing at the open boundaries, reconstructed from elevation and velocity harmonics of 21 tidal constituents, including the 8 primary constituents (M2, S2, N2, K2, K1, O1, P1, Q1), derived from the OSU TPXO9.5 global ocean tidal model, which offers a 1/30° resolution (Egbert et al., 1994). For the residual currents, we impose depth-averaged velocity and sea surface elevation from daily averaged ocean physics reanalysis of the North-West European Shelf provided by the Copernicus Marine Service (CMEMS) at resolution of $0.111° \times 0.067°$. We then combine these depth-averaged velocities and sea surface elevations from CMEMS and those reconstructed from TPXO model on the model's open boundary conditions.

Freshwater inputs on the circulation patterns are considered by adding rivers discharges in the model. In the model set-up, the Scheldt estuary receives its river discharge at the tail of the schematized upstream open boundaries. Observed discharge data for the Scheldt is sourced from the Schelde Monitor Portal, with a 10 min resolution. In addition, the discharges from major rivers such as the Thames, Seine, Meuse, and Rhine are imposed at their respective coastal outlets in the North Sea. These rivers are commonly included in models focusing on the Scheldt estuary and its immediate North Sea coastal surroundings (Gourgue et al., 2009; de Brye et al., 2010; Ivanov et al., 2020). The daily discharges imposed in the model for those rivers are sourced from the GEOGloWS model provided by ECMWF Streamflow Service.

2.3.3 Atmospheric forcing

We use outputs from the regional atmospheric model MAR (version 3.14) (Grailet et al., 2024), for 'Modèle Atmosphérique Régional' in French, as atmospheric forcing. MAR is a hydrostatic model based on the primitive equations, with convection parameterized following (Bechtold et al., 2001). The model has been applied in various areas such as polar regions (Gallée and Schayes, 1994; Fettweis et al., 2013, 2017), temperate region (Brasseur, 2001) tropical regions (Brasseur et al., 1998; Ridder and Gallée, 1998) and Belgium (Wyard et al., 2017). The advantage of using a regional over a global model lies primarily in its ability to provide more detailed simulations (in time and in space) for a specific geographic area to resolve small-scale processes. Here, we use MAR to simulate the atmospheric circulation over November and December 2013 at five different spatial resolutions: 2 km, 5 km, 10 km, 20 km and 30 km (Fig. 2.b-f). This allows us to compare the effect of the spatial resolution of the forcing atmopsheric model, from (sub)-regional to global scale resolutions. The 30 km resolution matches the ERA5 Reanalysis dataset scales (Hersbach et al., 2020) which was used as 6 hourly forcing of the MAR simulations. The sea surface temperature from ERA5 is prescribed in MAR over North Sea and temperature, wind, humidity as well as surface pressure from ERA5 are used at the lateral boundaries of the five MAR integration domains centered over the studied area. The atmospheric pressure and near-surface wind speed computed with MAR for all spatial resolution, are available at a 15 min time resolution. To assess the influence of the temporal resolution, we downscale the MAR output time to hourly, 3-hourly, and 6-hourly intervals by averaging, while maintaining constant spatial resolutions. This approach allows us to differentiate the effects of spatial resolution and temporal resolution. A summary of the data and atmospheric forcing condition used is given in Table 1.

Table 1. Summary of the forcing data used in the simulations.

	Area of application	**Source**	**Resolution**	
			Temporal	**Spatial**
Bathymetry	NWCS	EMODnet (2021)	-	115 m
	From Dutch coast to Scheldt Lower estuary	Rijkwaterstaat (2021)	-	20 m
	Scheldt upper estuary	AGENTSCHAP MDK (2021)	-	10 m
Oceanic forcing				
Large scale currents	Shelf boundary	NEMO (CMEMS)	1 day	0.111° × 0.067°
Tides	Shelf boundary	TPXO9.5	15 min	1/30°
Continental forcing				
Rivers discharge	Scheldt upstream boundary	Schelde Monitor	10 min	-
Rivers discharge	Thames, Seine, Rhine, Meuse river mouths	Geoglows (ECMWF)	1 h	-
Atmospheric forcing	Full domain	MAR	15 min - 1 h 3 h - 6 h	2 km - 5 km - 10 km 20 km - 30 km

2.4 Model-data comparison

We use various error metrics to assess the quality of our model results compared to observations from the different stations (see locations in Fig. 1). Let o and m represent the observed and modeled values, respectively, for a time series consisting of N data points. The mean of the observed time series is denoted by $\overline{o}$, and the mean of the modeled time series is denoted by $\overline{m}$. The performance metrics used to evaluate the model are summarized in Table 2. Observations include several types of data: wind speed, atmospheric pressure and water elevation. Water elevation data were sourced from Rijkswaterstaat data, providing continuous 10 min observation data along the Scheldt estuary . Wind speed and atmospheric pressure were acquired from the Flemish Banks Monitoring Network and located in the Belgian Continental Shelf, Meetnet Vlaamse Banken, with resolution of 10 min. In addition to the metrics listed in Table 2, we assess the performance of the model to simulate the peak in the sea level by computing the mean absolute error (MAE) for the highest water elevation value during the storm surge.

3 Results

Here, we analyze simulation results from November 20 to December 20, 2013, and more specifically on the passage of Xaver Storm on the December 5, 2013 (Fig. 2(a)). We begin by assessing quality the atmospheric forcing that we use in the model output of MAR model. Then, we validate the hydrodynamic simulation during the Xaver storm event, ensuring its reliability for subsequent analysis. For clarity, we present the results obtained using the highest temporal and spatial resolutions for atmospheric forcing: 2 km and 15 min. Finally, we analyze the influence of varying temporal and spatial resolutions in the atmospheric forcing on the hydrodynamic response, highlighting their impact on the quality of the of the storm surge simulation.

Table 2. Model performance metrics.

Metrics	**Description**	**Formula**
Mean Absolute Error	Magnitude of errors in a set of predictions to over/underestimate observation	MAE $= \frac{1}{N}\sum_{i=1}^{N}\lvert m_i - o_i\rvert$
Root Mean Square Error (RMSE)	Overall goodness-of-fit of the model and variability	$RMSE = \sqrt{\frac{1}{N}\sum_{i=1}^{N}(m_i - o_i)^2}$
Standard Deviation (σ_m)	Dispersion of model results around the mean	$\sigma_m = \sqrt{\frac{1}{N}\sum_{i=1}^{N}(m_i - \overline{m})^2}$
Correlation Coefficient (R)	Degree of agreement between modeled and observed data	$R = \frac{\sum_{i=1}^{N}(m_i - \overline{m})(o_i - \overline{o})}{\sqrt{\sum_{i=1}^{N}(m_i - \overline{m})^2 \sum_{i=1}^{N}(o_i - \overline{o})^2}}$

3.1 The atmospheric forcing

The high-resolution atmospheric model with spatial resolutions of 2 and 5 km (Fig. 2b-c) captures finer detail of the wind speed variability, particularly over continental regions, where the complex topography induces localized wind patterns. These higher resolutions exhibit pronounced variability compared to the smoother, more uniform wind fields observed over marine areas. As the spatial resolution coarsens to 10-30 km (Fig. 2d-f), fine-scale variations are increasingly smoothed out, with larger grid cells averaging localized phenomena. Although proving that finer spatial resolution universally improves simulation quality is challenging as spatially distributed observation would be needed for proper validation, these results illustrate the ability of higher resolutions to resolve mesoscale features, particularly in coastal and estuarine environments.

The atmospheric model MAR effectively reproduces the variability in atmospheric pressure and wind velocity during the simulated period, as shown by comparisons between MAR simulations with a 2 km spatial resolution and 15 min temporal resolution, and observations recorded at the Zeebrugge Dam Instrument (ZDI, Fig. 3). Similar consistency emerges across other spatial and temporal resolutions. This validation relies on observations from a single site. Additional locations are available in the area of interest, but they were excluded due to their proximity to the ZDI (within 10 km, hence smaller than the coarsest spatial resolution of the atmospheric model), or incomplete data for the study period. During the analysis period, three pronounced peaks in wind speed and corresponding drops in atmospheric pressure occurred. The first event, on November 28, corresponds to Storm Oskari; the second, on December 6, to Storm Xaver; and the third, on December 18, to Storm Bernd. Notably, among the three events, only Storm Xaver generated a significant storm surge in the region. In contrast, although Storm Bernd caused a more substantial drop in atmospheric pressure at the observation site, its relatively weaker wind speeds were insufficient to trigger a storm surge event.

We compute the RMSE values for wind speed and atmospheric pressure at ZDI across varying spatial and temporal resolutions, as summarized in Table 3. For wind speed, higher spatial resolutions generally enhance accuracy, with RMSE values ranging from 2.126 m/s at 2 km to 2.402 m/s at 20 km, with temporal resolution fixed at 15 min. However, the increasing trend of RMSE is not strictly monotonic as the spatial resolution coarsens, as intermediate resolutions, such as 10 km and 30 km, yield lower RMSE values than 5 km and 20 km, respectively. For atmospheric pressure, a portion of the RMSE is attributed to a systematic bias caused by the elevation difference between MAR (sea level) and the ZDI weather station. To account for this, we remove the mean bias and compute the centered RMSE (CRMSE) instead of the standard RMSE. The CRMSE increase with coarser spatial resolutions, ranging from 1.972 hPa at 5 km to 2.918 hPa at 20 km, also at a fixed 15 min temporal resolution. A similar non-monotonic pattern emerges, with the best performance at 5 km and slightly lower RMSE at 30 km compared to 20 km. The spatial resolution yielding the lowest CRMSE occurs at 5 km, while 30 km shows lower CRMSE than 20 km. Temporal resolution also impacts accuracy, with RMSE for both wind speed and atmospheric pressure increasing as the temporal resolution decreases from 15 min to 6 h, while spatial resolution is held constant at 2 km. Wind speed RMSE increases from 2.126 m/s to 2.263 m/s, while atmospheric pressure CRMSE rises from 2.623 hPa to 2.760 hPa. The differences in RMSE values across the different resolutions remain modest, with the mean RMSE for wind speed magnitude and atmospheric pressure at 2.218 m/s and 1.464 hPa, the maximum difference between the best and worst resolutions is 0.276 m/s for wind speed and 0.452 hPa for atmospheric pressure.

The RMSE values for both wind speed and atmospheric pressure remain lower than the standard deviation of observations, 7.474 hPa for atmospheric pressure and 3.512 m/s for wind speed, indicating that biases introduced by resolution changes are not statistically significant and the model errors are within the expected natural variability. To quantify these variations, we compute the RMSE as a fraction of standard deviation of observations, relative RMSE (RRMSE) in Table 3. For wind speed, the RRMSE ranges from 0.605 at 2 km, 15 min resolution to 0.684 at 20 km, 15 min resolution, while for atmospheric pressure, it varies from 0.264 at 5 km, 15 min resolution to 0.390 at 20 km, 15 min resolution. These percentages suggest that the differences in RMSE across resolutions fall within the natural variability of atmospheric conditions at ZDI, meaning that the model's sensitivity to resolution changes is minimal.

The correlation coefficients in Table 3 show a good agreement between the MAR model results and observations. For wind speed at different spatial resolutions, correlation ranges from 0.780 at 20 km to 0.835 at 5 km, with finer spatial resolutions generally improving agreement, though not in a strictly monotonic manner, similar to RMSE trends. Atmospheric pressure exhibits consistently high correlation values above 0.993 across all spatial resolutions, demonstrating strong model fidelity. Temporal resolution mainly affects wind speed correlation, decreasing from 0.826 at 1 h resolution to 0.785 at 6 h resolution at 2 km spatial resolution. In contrast, atmospheric pressure correlation remains above 0.984, suggesting that pressure variations are less sensitive to temporal smoothing compared to wind variation.

Table 3. Statistics for wind speed and atmospheric pressure with different MAR spatial and temporal resolutions at Zeebrugge Dam Instrument (ZDI) from November 25 to December 20, 2013.

MAR spatial and temporal resolutions	Wind Speed			Atmospheric Pressure		
	RMSE [m/s]	RRMSE [-]	Correlation [-]	CRMSE [hPa]	RRMSE [-]	Correlation [-]
2 km, 15 min	2.126	0.605	0.818	2.443	0.327	0.996
5 km, 15 min	2.350	0.669	0.835	1.972	0.264	0.996
10 km, 15 min	2.131	0.607	0.803	2.698	0.361	0.996
20 km, 15 min	2.402	0.684	0.780	2.918	0.390	0.995
30 km, 15 min	2.165	0.616	0.802	2.510	0.336	0.993
2 km, 1 h	2.140	0.609	0.826	2.637	0.353	0.996
2 km, 3 h	2.163	0.616	0.816	2.623	0.351	0.994
2 km, 6 h	2.263	0.644	0.785	2.760	0.369	0.984

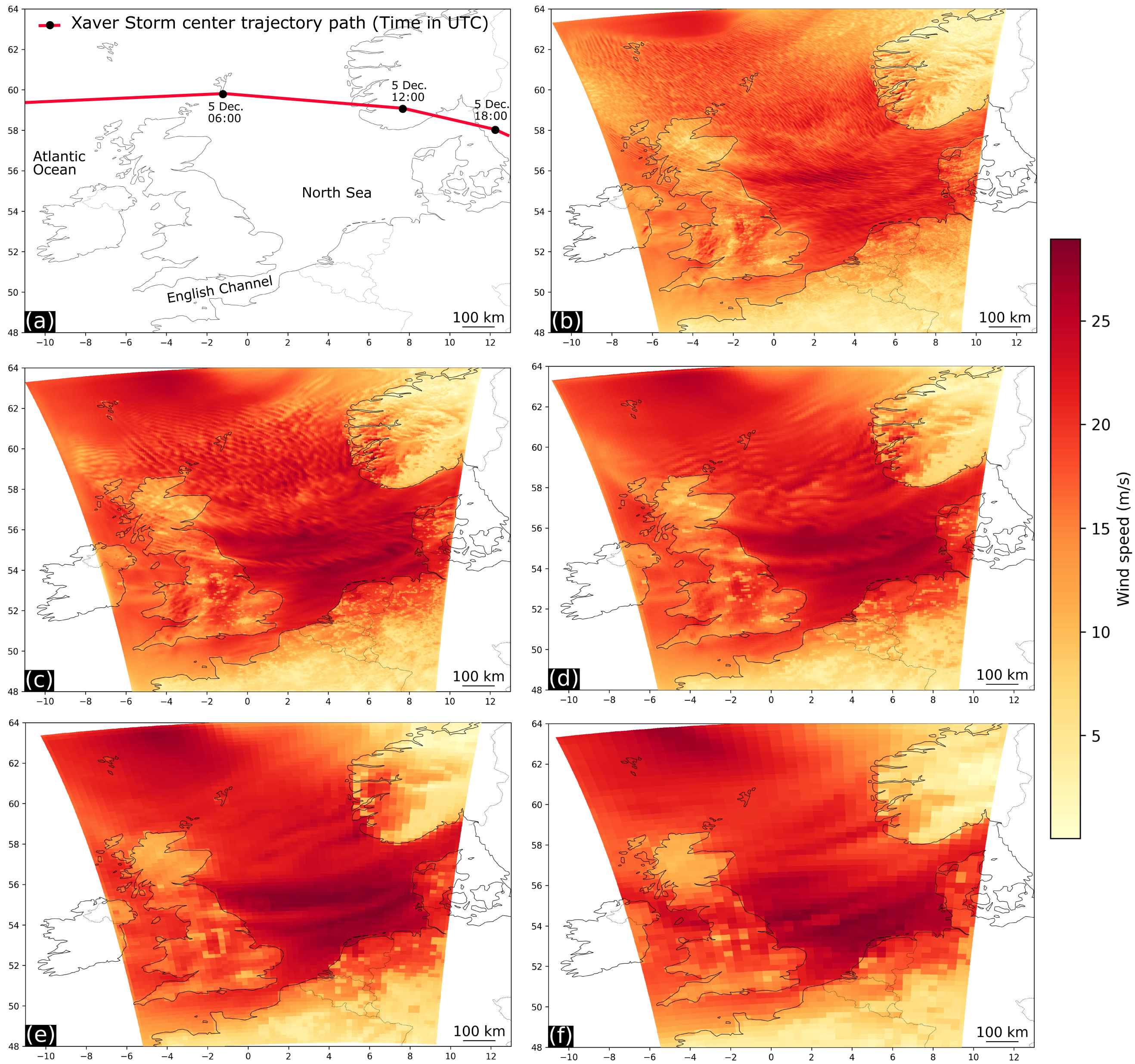

Figure 2. (a) Storm Xaver's central low-pressure trajectory over the North Sea and surrounding areas, showing its path on December 5, 2013, with time stamps in UTC. The trajectory is marked with a red curve. Panels (b–f) display snapshots of wind velocity magnitude during the storm's passage, specifically at 12:00 UTC on December 5, 2013, derived from the MAR atmospheric model at various spatial resolutions. These resolutions range from (b) 2 km, (c) 5 km, (d) 10 km, (e) 20 km, to (f) 30 km.

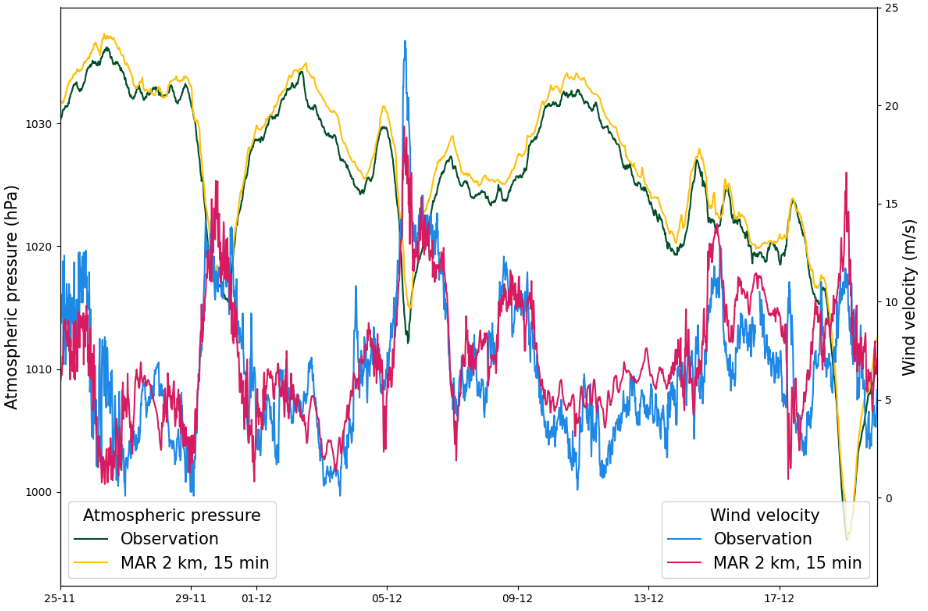

Figure 3. Wind velocity and atmospheric pressure at Zeebrugge Dam Instrument (ZDI) from November 25 to December 20, 2013, showing observations in green for atmospheric pressure and blue for wind velocity, alongside MAR atmospheric model outputs at 2 km and 15 min resolution, represented in yellow for atmospheric pressure and red for wind velocity.

3.2 Ocean model validation during storm surge

The time series analysis obtained from the model and tide gauges show that the model accurately reproduces the tidal cycles at the different stations (see illustration for water elevation in Fig. 4). There is a slight underestimation of the tidal height and low tide by about 0.1 m but these deviations are relatively minor as compared to the tidal range of about 6 m. Error metrics further indicate the model's robustness (Table 4). The bias values remain near zero and the correlation coefficients, consistently exceeding 99%, confirm a strong linear agreement between the modeled and observed water elevations. This high correlation underscores the model's effectiveness in capturing the dynamics of water elevation within the estuary. The RMSE values, ranging from 0.221 m at Westkapelle to 0.297 m at Antwerpen Loodsgebouw, where the tidal amplitude is around 4 m.

3.3 Storm surge simulation sensitivity to atmospheric model resolution

The comparison of simulations using atmospheric forcing at different spatial resolutions, while maintaining a fixed temporal resolution, indicates that the best results are achieved with the 2 km resolution (Fig. 5). The performance of peak water level modeled declines as the spatial resolution of atmospheric forcing decreases. Along the Scheldt estuary the finer spatial resolution consistently outperforms other resolutions in modeling the maximum water elevation, named hereafter as the peak water or peak surge, particularly in upstream stations (Fig. 5). The results of 5 km and 10 km resolutions are close to the accuracy of the 2 km forcing, whereas coarser resolutions of 20 km and 30 km yield significantly poorer results. As a result, there is 20% improvement in peak water elevation estimation between the simulations forced at 2 km and 30 km resolution in upstream regions like Antwerpen Loodsgebouw and Kallosluis Schelde.

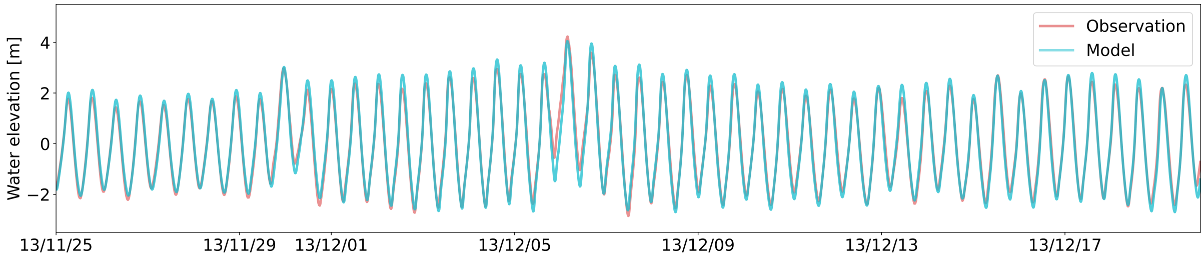

Figure 4. Sea surface elevation at Hansweert as simulated by SLIM with atmospheric forcing of 2 km spatial and 15 min temporal resolutions of MAR (blue) compared to observations (red), time series from November 25th to December 20th 2013.

Table 4. Error metrics for the different stations measurement along the Scheldt estuary, from November 25 to December 20, 2013.

Station	RMSE [m]	Correlation [-]	MAE [m]
Vlakte van de Raan	0.223	0.985	0.174
Cadzand	0.218	0.987	0.166
Westkapelle	0.213	0.986	0.163
Breskens Veerhaven	0.214	0.988	0.161
Vlissingen	0.219	0.988	0.166
Gat van Borssele	0.226	0.989	0.171
Hansweert	0.238	0.990	0.180
Walsoorden	0.242	0.990	0.185
Baalhoek	0.245	0.990	0.187
Schaar van de Noord	0.245	0.991	0.187
Prosperpolder	0.255	0.991	0.194
Fort Liefkenshoek	0.249	0.991	0.188
Kallosluis Schelde	0.262	0.990	0.199
Antwerpen Loodsgebouw	0.297	0.987	0.232

The comparison of the simulations obtained by forcing the hydrodynamic model SLIM with MAR at different temporal resolutions and fixed spatial temporal resolution shows that the best results are obtained with the 15 min resolution. However, the impact of the temporal resolution of the atmospheric forcing on the peak water levels is obvious only at the finest 2 km spatial resolution (Fig. 6.a). The temporal resolution of the atmospheric forcing appears to have an almost negligible impact on the quality of model simulations when spatial resolution is coarser (Fig. 6.b). At 5 km resolutions (Fig. 6.b), the scatter of points across different temporal resolutions shows comparable performances across most stations, with no evident advantage for higher temporal resolution. Similarly, coarser spatial resolutions ranging from 10 to 30 km (not shown here) exhibit behavior comparable to the 5 km resolution. The results suggest that the temporal resolution of the atmospheric forcing only has an impact on the model's performance when the spatial resolution is finer.

The deviation in peak water levels with a fixed temporal resolution of the atmospheric forcing increases as the spatial atmospheric forcing resolution becomes coarser across the domain (Figs. 7). This deviation peak is defined as the difference between the maximum water elevation of two simulations. The peak deviation between the simulations forced with 2 km and 5 km atmospheric resolutions (Figs. 7.a) shows value of ± 10 cm. As the resolution coarsens to 10 km, 20 km, and 30 km (Figs. 7.b-d), the deviations expand both in magnitude and spatial extent. Deviations remain modest between the 2 km and 5 km simulations, mostly under 10 cm (Fig. 7.a), but exceed 10 cm over the center area of the lower estuary as the resolution further decreases (Figs. 7.b-d), with maximum deviations approaching 40 cm in the center of the Scheldt lower estuary when comparing with simulation using 30 km resolution. The Scheldt estuary exhibits the largest deviations, with the center of the lower estuary and coastal region showing the most sensitivity to resolution changes while the North Sea shows smaller deviations, reflecting reduced sensitivity in regions farther from the estuary's funnel-shaped topography.

The regions experiencing significant deviations in peak water levels expand as the temporal resolution of the atmospheric forcing becomes coarser. The deviation in peak water levels, at a fixed spatial resolution, exhibits variations of approximately ±10 cm between the simulation forced at 15 min and the other temporal resolution (Figs. 8). This pattern is particularly noticeable in the Scheldt estuary, where the close-up views (Figs. 8 b,d and f) highlight substantial differences of the area with larger peak differences. The area experiencing large deviations in peak water levels expands further in the North Sea, where the spatial extent of areas with large deviations in peak water levels also increases with coarser temporal resolution (Figs. 8a,c and e). Additionally, a distinct shift in the sign of the deviation is observed, dividing the North Sea and the English Channel. Compared to simulations at coarser resolutions, the simulation using the reference atmospheric forcing resolution of 2 km yields higher peak water levels (positive deviation) on the Scheldt estuary and North Sea and lower peak water levels (negative deviation) on the Channel.

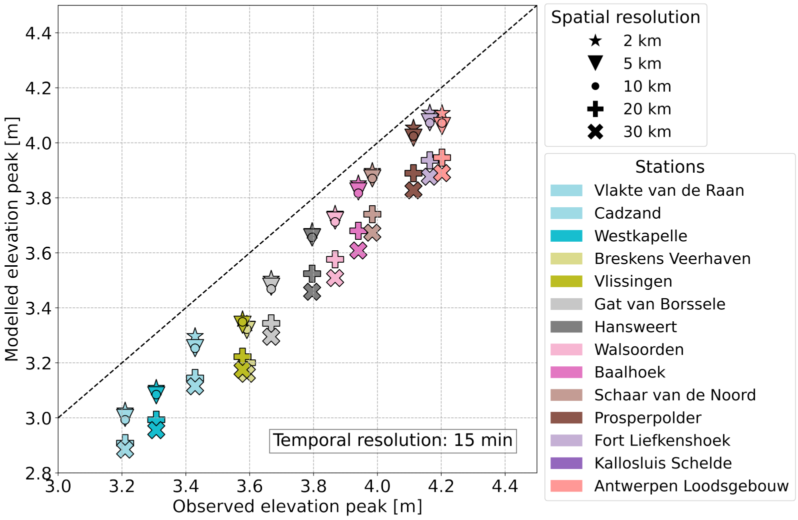

Figure 5. Comparison of peak water elevation between simulation (y-axis) and observation (x-axis) at various stations and spatial resolution, using MAR atmospheric forcing fixed at 15 min temporal resolution. Different symbols indicate spatial resolutions of the atmospheric forcing (ranging from 2 km to 30 km), and colors correspond to specific coastal stations as shown in the legend. The dashed line represents perfect agreement between model predictions and observations. The best agreement between model and observation is achieved for the largest storm surge peaks and the finest spatial resolution.

The hydrodynamic model results better agree with observations at upstream stations, where surge levels are highest. This holds true across different temporal and spatial resolution of the atmospheric forcing. Stations such as Prosperpolder and Antwerpen Loodsgebouw

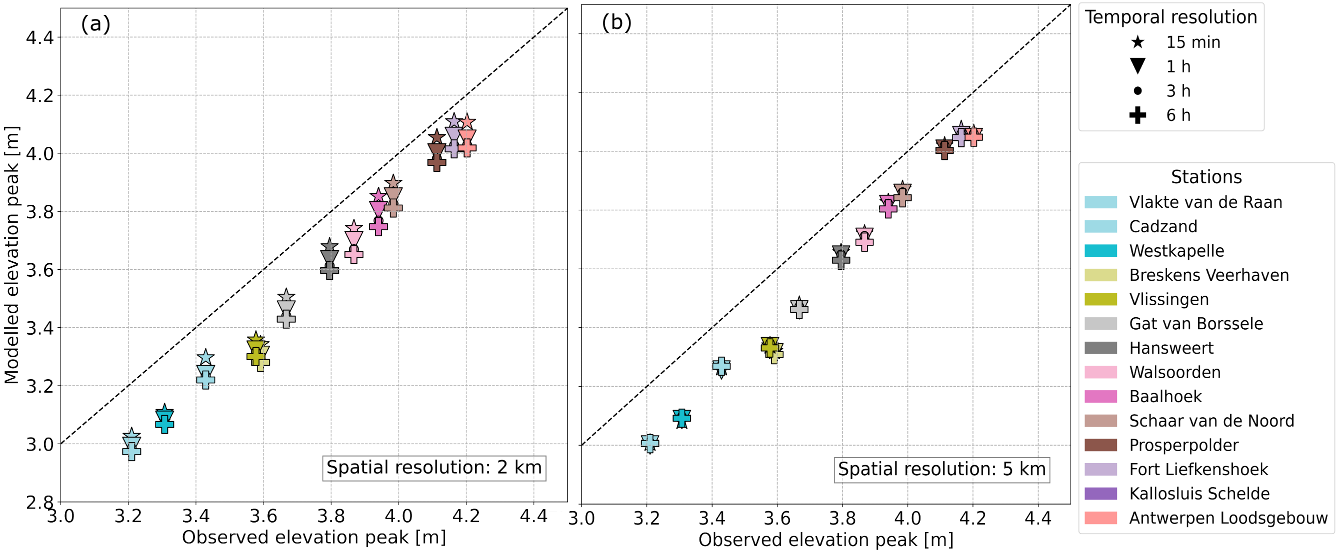

Figure 6. Same as Fig. 5 for various temporal resolution of the atmospheric forcing with spatial resolution fixed at (a) 2 km, (b) 5 km. Symbols represent various temporal forcing resolutions, ranging from 15 min to 6 hours. A finer spatial resolution of 2 km (a) demonstrates significant improvement with increased temporal resolution compared to the coarser spatial resolution of 5 km (b).

exhibit slightly greater discrepancies in peak surge levels, as evidenced by scatter markers deviating further from the diagonal line at coarser atmospheric resolutions. These deviations become more pronounced as resolution of atmospheric forcing decrease, as shown in Figs. 7 and 8. At the most upstream stations, temporal resolution exerts a substantial influence on peak water elevations, with observed differences of up to 15 cm between simulation forced at 15 min and 6 h temporal resolution (Figs. 6.a and 8). Spatial resolution has an even greater impact, causing a peak surge deviations of up to 30 cm between 2 km and 20 km resolutions (Figs. 5 and 7) at those stations.

The timing of the storm surge is largely unaffected by the resolution of the atmospheric forcing, as peak water levels occur nearly simultaneously across most of the domain, regardless of the spatial or temporal resolution of the forcing. Peak water levels across different spatial and temporal resolutions display a time variation mostly around 0 min of deviation with a range within ± 10 min (Figs. 9 and 10). Both spatial and temporal scales exhibit similar patterns. The higher value of deviations appear as patchy regions in the estuary and coastal areas. These regions become larger as spatial or temporal resolution of the atmospheric forcing gets coarser, particularly in the Estuary but it stays in the limited range of 10 min. Also in the estuary, a large time variation, with blue and red patches, can be seen in the region with tidal marshes.

4 Discussion and conclusions

The quality of a storm surge simulation is sensitive to atmospheric forcing spatial and temporal resolution, particularly in topographically confined areas like estuaries. By forcing a multiscale hydrodynamical model with atmospheric forcing at different spatial resolutions ranging from 2 km to 30 km and temporal resolutions from 15 min to 6 h, we highlighted this impact for the Scheldt estuary-sea continuum during the major storm Xaver. Our model was able to reproduce the dynamics of the storm surge event, with errors similar to other studies (e.g.

https://doi.org/10.5194/egusphere-2025-634
Preprint. Discussion started: 21 February 2025

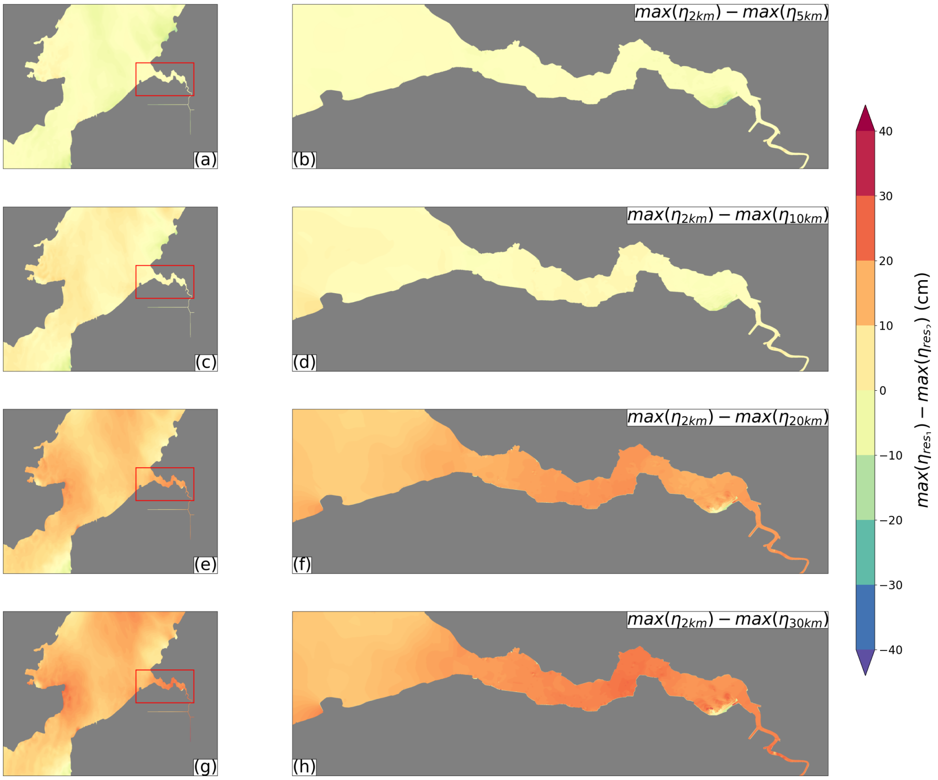

Figure 7. Difference in maximum water elevation between simulation results at 2 km atmospheric forcing resolution and those at (a-b) 5 km, (c-d) 10 km, (e-f) 20 km, and (g-f) 30 km forcing resolutions. The temporal resolution of the atmospheric forcing is fixed at 15 min for all simulations. two simulations with varying spatial resolutions. The left panels depict the coastal North Sea, while the right panels present close-up views on the Scheldt estuary.

Plancke et al. (2020)). We found that increasing the spatial resolution of the atmospheric forcing led to more accurate predictions of peak surge levels. In contrast, coarser resolutions tended to underestimate the peak surge elevation. While the temporal resolution also influenced the results, its impact was noticeable only for the finer spatial scales and its impact diminished with coarser resolutions. Overall, our analysis shows that spatial resolution plays a more significant role than temporal resolution in improving the accuracy of peak surge modeling in estuarine region.

The magnitude of the modeled storm surges across the Scheldt estuary is highly sensitive to the resolution of atmospheric forcing, a finding that aligns with previous studies, such as Agulles et al. (2024). However, while previous studies emphasized the role of temporal resolution at larger spatial scales, our results indicate that spatial resolution has a stronger influence when modeling estuarine environments at finer scales. This contrasts with the findings of the aforementioned study for which temporal resolution played a more significant role than spatial resolution at scales of 1.5–25 km and temporal resolutions ranging from hourly to daily. This divergence in results may be because Agulles et al. (2024) focused primarily on larger-scale coastal dynamics using atmospheric data at broader spatial and temporal scales, on the continental scale along the European coastline and on several decades, while our study concentrated on the finer-scale dynamics of

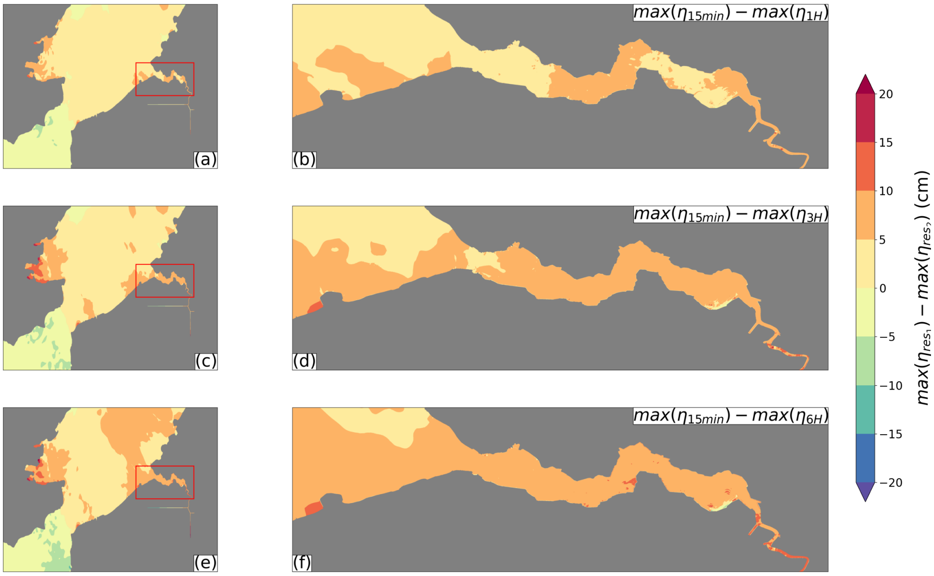

Figure 8. Difference in maximum water elevation between simulation results at 15 min atmospheric forcing resolution and those at (a-b) 1 h, (c-d) 3 h, (e-f) 6 h forcing resolutions. The spatial resolution of the atmospheric forcing is fixed at 2 km for all simulations. The left panels depict the coastal North Sea, while the right panels present close-up views on the Scheldt estuary.

estuarine regions and smaller temporal scale. Furthermore, our use of a different atmospheric data source from them may have contributed to these contrasting results. While Agulles et al. (2024) found optimal results using the ERA5 Reanalysis Dataset at an hourly resolution with a 31 km spatial scale (Hersbach et al., 2020), our study suggests that such resolutions underperform in estuarine environments, where finer spatial scales yield more accurate storm surge modeling. The determination of appropriate spatial resolution for atmospheric forcing is ultimately dependent on the specific processes and scales being modeled. For coastal storm surge dynamics, which typically unfold over several kilometers and hours, atmospheric forcing at spatial scales of tens of kilometers may suffice (Agulles et al., 2024; Meyer and Gaslikova, 2023; Muller et al., 2014; Ridder et al., 2018). However, our results indicate that these standard resolutions may be inadequate for modeling storm surges in estuarine regions, where finer atmospheric forcing is necessary to capture the more complex dynamics at play in a more confined environment.

Improving storm surge modeling through higher-resolution model necessitates to balance the benefits of increased accuracy and the associated computational and practical costs. This demand concerns both computing the high-resolution atmospheric model and the hydrodynamic model. Our findings demonstrate that higher temporal resolution of the atmospheric forcing (15 min), when paired with the finest spatial resolution of the atmospheric forcing (2 km) provides the best results for the peak surge simulated by the hydrodynamic model. However, this raises the question of how much further refinement is both feasible and beneficial. First, for the temporal resolution of the atmospheric forcing: could higher resolution than 15 min could further refine the model result in the estuary? The surge takes around two hours to travel along the estuary, with peak water levels hitting Vlakte de Raan at 15:40 and Antwerp at 17:50 on December 6th. This 2 hours propagation time is eight times longer than our finest temporal resolution of the atmospheric forcing. Further increasing this temporal resolution may not significantly enhance results and could introduce model errors without providing meaningful gains in accuracy. Second, refining spatial

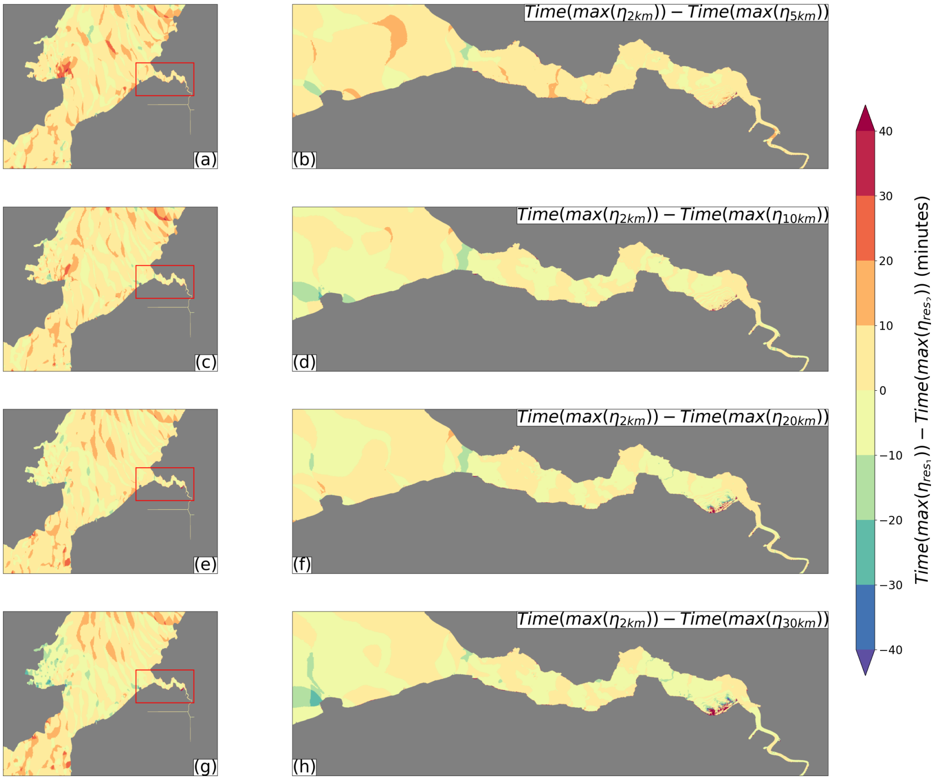

Figure 9. Timing differences in peak water levels during the storm surge between the reference simulation with 2 km resolution, and simulations with coarser spatial resolution: (a, b) 5 km, (c, d) 10 km, (e, f) 20 km, and (g, h) 30 km resolution, and a fixed temporal resolution of fixed to 15 min. The color scale indicates the deviation in peak timing from the reference, measured in minutes. The left panels depict the coastal North Sea, while the right panels present close-up views on the Scheldt estuary.

resolution of the atmospheric model poses its own challenges. Achieving finer spatial resolution from the atmospheric model comes with substantial computational costs and is constrained by the hydrostatic assumption of the atmospheric model, which restricts the ability to achieve spatial resolutions finer than about 2 km. Refining beyond this threshold would require non-hydrostatic atmospheric models, which are computationally intensive. Finally, spatial resolution of the computational mesh also significantly impacts model outcomes. In this study, the coarsest mesh element was designed to align with the finest atmospheric spatial resolution of 2 km. If more detailed atmospheric forcing becomes available, a correspondingly finer computational mesh would be required. However, solving the hydrodynamics model on a finer mesh is much more computationally expensive and introduce challenges related to the mesh design, and can highly impact the accuracy of the hydrodynamic simulations (Saint-Amand et al., 2023). Future research should therefore focus on identifying an optimal trade-off between model accuracy and the practical limitations of computational resources. Balancing these factors to improve storm surge modeling while ensuring its feasibility for real-world applications.

Consistency in the timing of peak storm surges across various spatial and temporal resolutions is a another finding of this study. We found that the predicted timing of peak surge events remained relatively stable, regardless the resolution of the atmospheric model. This suggests

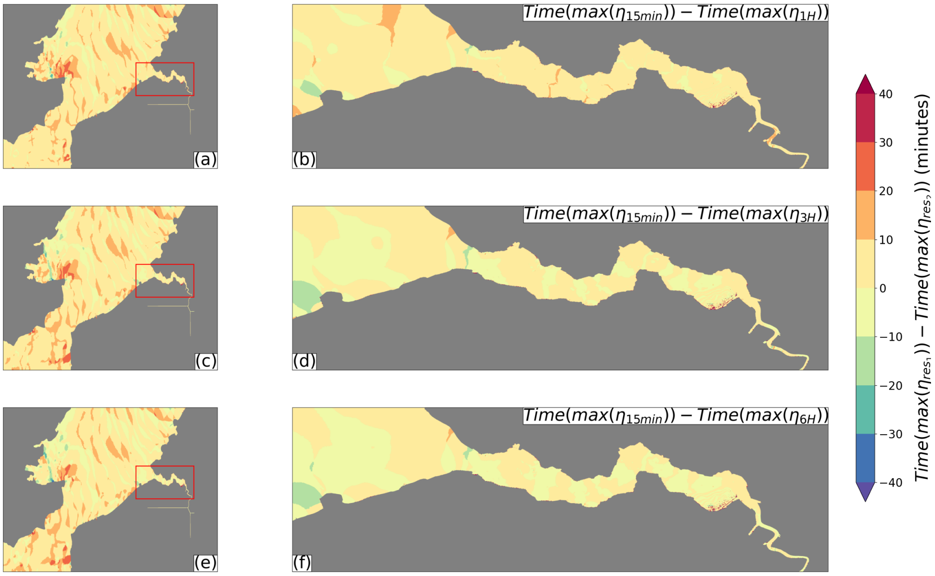

Figure 10. Timing differences in peak water levels during the storm surge between the reference simulation with 2 km resolution and 15 min atmospheric forcing, and simulations with coarser temporal resolution: (a, b) 1 h, (c, d) 3 h, and (e, f) 6 h intervals. The color scale indicates the deviation in peak timing from the reference, measured in minutes. The left panels depict the coastal North Sea, while the right panels present close-up views on the Scheldt estuary.

that factors beyond the spatial or temporal resolution of atmospheric forcing may be influencing the timing of peak surges. One plausible mechanism warranting further investigation is the modulation of surge timing by the tidal cycle. During the Xaver Storm, the peak surge event coincided with high tide, strongly implying that this synchronization played a role in shaping the observed timing. This alignment between storm surge peaks and specific tidal phases likely accounts for the consistent ±20 min accuracy in surge timing predictions observed across all model resolutions evaluated in this study. The interaction between tidal dynamics and storm surge timing has been analyzed in previous studies, supporting the significance of this relationship in shaping surge behavior (Al Azad et al., 2018; Thomas et al., 2019).

As with any modeling study, our approach has limitations and assumptions that should be acknowledged. Firstly, the use of a 2D model does not include the vertical density gradients, which can influence circulation and mixing processes in stratified estuaries. However, the Scheldt estuary and its coastal region is well-mixed due to strong tidal forcing which propagates up to 80 km upstream from the estuary mouth, reducing the impact of baroclinic effects typically associated with salinity and temperature variations (Van Damme et al., 2005; Ivanov et al., 2020). While the 2D model does not capture the full three-dimensional complexity, including baroclinic effects arising from salinity and temperature variations, it remains a valuable tool for understanding storm surge behavior under different spatio-temporal atmospheric forcings. We expect the influence of 3D baroclinic physics will further be limited compared to the impact of atmospheric resolution, as the flow dynamics during the storm surge events on this shallow region are primarily driven by wind, atmospheric pressure and tides. Additionally, the 2D model allows the use of a finer horizontal mesh resolution that would have been hardly usable in a 3D model. Another limitation of our study is the simplified representation of vegetation through increased bottom friction, which may not fully capture the frictional dynamics in shallow water environments. This simplification underestimates friction in areas where water depth is less than vegetation

https://doi.org/10.5194/egusphere-2025-634
Preprint. Discussion started: 21 February 2025

height, such as the Scheldt marshes, where plants can grow up to one meter. As depicted by the blue and red patches in Fig. 9. In reality, the drag exerted by vegetation should remain constant regardless of depth, but our model introduces variability, reducing drag as depth increases. More advanced methods, like those proposed by (Baptist et al., 2007), better capture vegetation's impact by accounting for its full drag effect. Future studies should adopt refined drag models to improve storm surge simulations, particularly in marshlands where vegetation mitigates extreme weather impacts (Hu et al., 2015).

Storm surge modeling in estuarine environments faces significant challenges due to complex atmospheric and hydrodynamic interactions. Our findings emphasize the importance of high-resolution atmospheric forcing for improving storm surge modeling in the estuary-sea continuum. As mentioned previously, ERA5 reanalysis provide hourly forcing at a spatial resolution of 31 km produced by ECMWF. Similarly, operational forecasts produced by ECMWF's Integrated Forecasting System (IFS) offer comparable spatial resolution but vary in temporal granularity, ranging from 1 h to 6 h. While these datasets represent significant progress, their resolutions remain insufficient to fully capture the fine-scale dynamics characteristic of estuarine regions. Climate change and associated sea level rise are expected to intensify storm surge events (Woth et al., 2006), underscoring the value of addressing these limitations. Enhancing the resolution of atmospheric forcing data has the potential to significantly improve model accuracy, ultimately informing effective coastal protection strategies. Achieving a balance between higher model resolution and computational efficiency is will allow to support both real-time forecasting and long-term planning. These advancements would contribute to enhance the resilience of river-estuary systems against evolving environmental threats.

Code and data availability. This project was carried out on multiple computers, including high-performance computing (HPC) systems and desktops. While we have chosen not to publicly release the code, it will be made available upon request.

Appendix A: Bathymetry sources

The domain's bathymetry (Fig. A1) was constructed using multiple sources with resolutions varying by region, from coarse in the Northwestern Continental Shelf (NWCS) to fine in the Scheldt estuary. High-resolution datasets, such as AGENTSCHAP MDK (2021) and Rijkwaterstaat (2021), were applied in the estuary, a constant bathymetry was used in the schematized upstream Scheldt river and coarser data from EMODNet was used elsewhere. All datasets were standardized to a consistent vertical datum to ensure coherence before being combined. The bathymetry resolution varies based on the geographical location, ranging from coarser (115 m) resolutions in the Northwestern Continental Shelf (NWCS) to finer (10 m) resolutions in the Scheldt estuary region. The process of combining and standardizing the datasets to a consistent datum level ensures coherence and accuracy in the simulation results. Finally, the bathymetry was interpolated onto the unstructured mesh, allowing for seamless transitions between resolutions and accurate representation of the estuarine system.

Appendix B: Model calibration

The final Manning roughness coefficients used in the simulation are illustrated in Fig. B1. A calibration of the model was conducted to achieve the best agreement with observed water levels and tidal components. This process involved iterative adjustments of Manning's values across different segments of the river-estuary-ocean continuum. The simulations performed for the calibration are described in Table B2. The calibration is done using a Taylor Diagram (Fig B2) which involves the correlation (R), standard deviation (σ), and centered root mean square error (CRMSE) between the simulated (m) and observed (o) data.

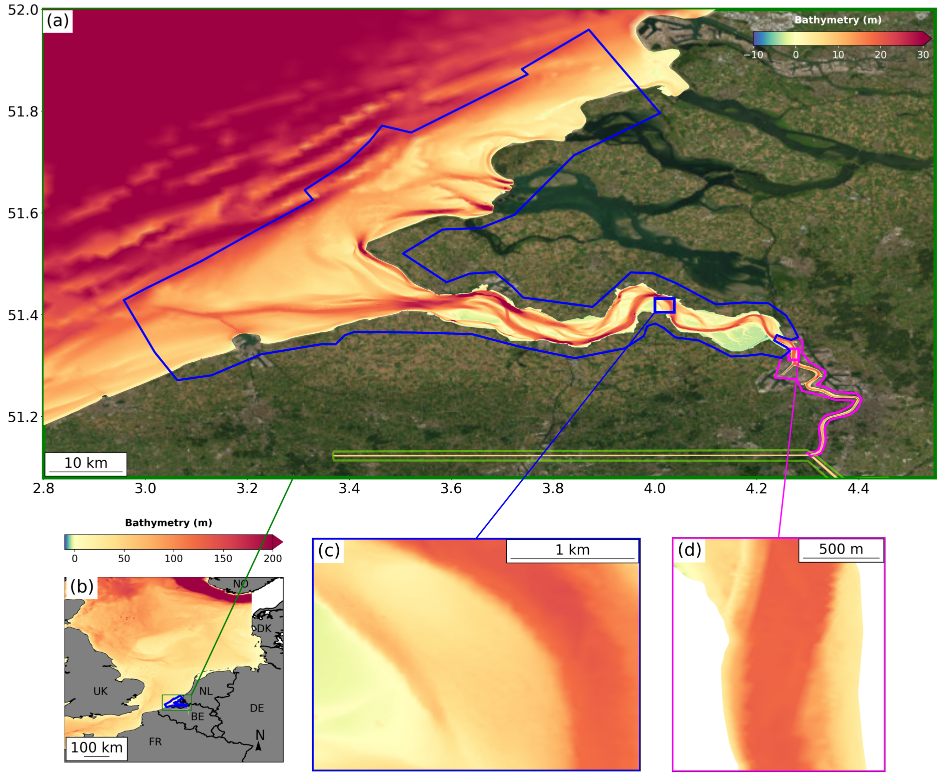

Figure A1. Interpolated bathymetry and source distribution across the model domain. Colored regions in panel (a) highlights the extend of the high-resolution bathymetric data sources used for the coastal area and lower Scheldt estuary from Rijkswaterstaat (2021) in blue, for the upper Scheldt estuary from AGENTSCHAP MDK (2021) shown in magenta, and the schematized freshwater tidal network with constant bathymetry in green and Esri World Imagery as basemap (ESRI, 2025). The lower panels illustrate the interpolated bathymetry mapped onto the computational mesh at (b) a large-scale view of the North Sea, and (c-d) close-up views of two specific locations within the Scheldt estuary. Panels on the estuary (a,c and d) share the same colorbar and panel on the North Sea (b) has its own.

Centered Root Mean Square Error (CRMSE) is an error metric that accounts for bias, $CRMSE = \sqrt{\frac{1}{N}\sum_{i=1}^{N}(m_i - o_i - \overline{m} + \overline{o})^2}$. Following Taylor (2001), CRMSE can be related to σ_m and R with the following relationship :

$$\mathrm{CRMSE}^2 = \sigma_o^2 + \sigma_m^2 - \sigma_o \sigma_m R. \tag{B1}$$

From law of cosines, a Taylor diagram can be visualized as a polar coordinate plot where $r = \sigma_m$ and $\theta = arcos(R)$. $CRMSE^2$ has units of the principal variable squared and CRMSE appears as the distance from the position of a perfect model ($r = \sigma_o, \theta = 0$). We can divide equation (B1) by σ_o and obtain dimensionless equation and the Normalized Taylor Diagram, this normalized Taylor Diagram is more suitable for comparing different data set from various source, thus with different variances. The normalized equation is:

$$CRMSE^{*2} = 1 + \sigma_m^{*2} - \sigma_m^* R,$$

https://doi.org/10.5194/egusphere-2025-634
Preprint. Discussion started: 21 February 2025

where $CRMSE^* = \frac{CRMSE}{\sigma_o}$ and the normalized standard deviation $\sigma_m^* = \frac{\sigma_m}{\sigma_o}$.

In the normalized diagram, the perfect model always lies at $(r,\theta) = (1,0)$, facilitating comparison of data sets with different variances, thus assessing the model performance at different observation point with various simulation set up.

The calibration results for the North Sea region are illustrated in figure B2 with the Taylor diagram of water elevation for simulations 1-4 of 15th June to 31st July. Along the coastal zone of the North-Sea and up to the Lower Scheldt Estuary, variations in the Manning coefficient impact the standard deviation of the water surface elevation. An increase in the Manning coefficient results in a leftward shift of the normalized standard deviation. The optimal Manning coefficient for the coastal North Sea is identified as 0.025 s $m^{-1/3}$.

We show here the calibration for the North Sea region (Fig. B2). The other areas showcase similar results and are not presented. Table B1 details the values of the correlation and normalized standard deviation for the simulations 1-4 at Cadzand.

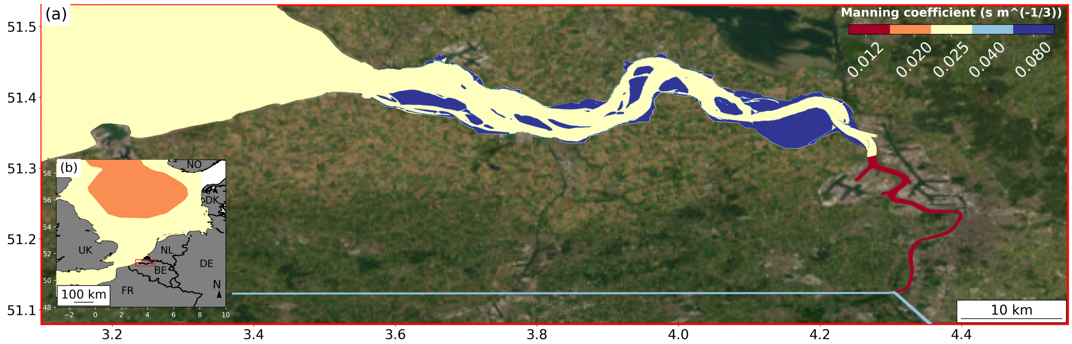

Figure B1. Manning coefficient distribution along (a) the Scheldt estuary, with Esri World Imagery as basemap (ESRI, 2025), and (b) the North Sea.

Table B1. Correlation and Normalized Standard Deviation values when comparing water elevation at Cadzand for simulation n°1-4.

$n[sm^{-1/3}]$	$\sigma_m[-]$	$R[-]$
0.026	1.0036	0.9937
0.025	1.0038	0.9937
0.024	1.0398	0.9935
0.023	1.0394	0.9935

Appendix C: Wetting and Drying scheme

The goal of the WD algorithm is to ensure that the water depth $H = \eta + b$ remains strictly positive. Various WD methods exist, both in explicit and implicit schemes. Explicit methods must satisfy to the Courant–Friedrichs–Lewy (CFL) criterion, limiting time steps and increasing computational costs for large-scale simulations. Implicit methods allow larger time steps but may disrupt mass and momentum conservation. The first implicit method developed with SLIM considered element removal algorithm to classify and remove dry elements, which can destabilize simulations (Kärnä et al., 2011). A second implicit method employed a thin film layer algorithm to maintain positive water depths,

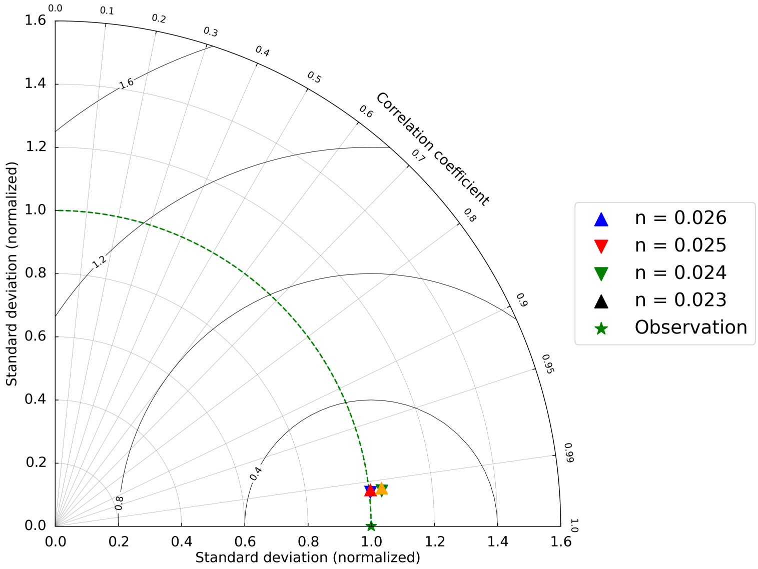

Figure B2. Taylor diagram comparing water elevation for the simulations n°1-4 (n=0.023-0.026) at Cadzand.

Table B2. Parameters for each simulation for the calibration

Simulation	**Period**	**Manning coefficient [$sm^{-1/3}$]**		
numbers		**North Sea**	**Lower estuary**	**Tidal marshes**
1-4	15 Jun.- 31 Jul. 2013	0.023-0.025	0.012	0.08
5-12	15 Jun.- 31 Jul. 2013	0.025	0.008-0.015	0.08
13-16	15 Jun.- 31 Jul. 2013	0.025	0.015	0.06-0.10

though it complicated parametrization due to its multiple requirements (Le et al., 2020). SLIM optimized on GPUs has greatly improved explicit performance, allowing a turn to explicit schemes which showcase simpler parametrization. This code guarantees a minimum water depth H_{thin} to be maintained in each element. This limiter ensures that the water depth H does not approach zero, preventing numerical instabilities. The temporal scheme in the model operates as follows:

$$U^{n+1} = U^n + \Delta t M^{-1} F(U^*)$$

where U^* is an intermediate state depending on the Runge-Kutta scheme, in this case, with an explicit Euler scheme, $U^* = U^n$, F represents the flux and M is the mass matrix. For mass conservation, the scheme is:

$$\eta^{n+1} = \eta^n + \Delta t M^{-1} F(\eta^*, \mathbf{u}^*) \qquad \text{(C1)}$$

To account for numerical rounding errors, the scheme is designed to maintain $H > H_{\text{thin}}$. The value of H_{thin} is selected between 10^{-4} and 10^{-3} for single precision, and between 10^{-9} and 10^{-12} for double precision.

F can further be decomposed into the internal and external fluxes:

$$F = F^{\text{int}} + F^{\text{ext}}$$

For wetting and drying purposes, F^{int} is less relevant since it merely transfers mass between vertices. The crucial part is F^{ext}, the flux entering and leaving the triangle. The wetting and drying scheme involves four steps, each of them will be described in more details afterwards:

1. Compute the fraction of F^{ext} that exits the triangle.
2. If excessive mass is leaving the triangle, compute a limiting coefficient to reduce the flux, ensuring $H > H_{\text{thin}}$ on average.
3. Compute all fluxes using the limiting coefficient.
4. Ensure $H > H_{\text{thin}}$ at each vertex. If $H < H_{\text{thin}}$ at any vertex, apply a limiter and redistribute the mass within the triangle.

Thus, F^{ext} is computed as an integral F^{e_i} over each edge i of a triangle:

$$F^{\text{ext}} = F^{e_1} + F^{e_2} + F^{e_3}$$

Each of these integrals is evaluated numerically as a weighted sum of the fluxes computed at the edge's integration points. When calculating external fluxes, the flux direction is assessed at each integration point. After determining the outgoing external flux $F^{\text{ext,out}}$, the total mass variation is:

$$\Delta V = \sum_{i \in \text{nodes}} F_i^{\text{ext,out}}$$

Let $\tilde{H}_i = \eta_i^n + b_i - H_{\text{thin}}$, which represents the water column height at node i that can be safely removed. The total volume that can be safely removed is then given by:

$$V = \sum_{i,j \in \text{nodes}} M_{ij} \tilde{H}_j^n = \frac{J}{6} \sum_{i \in \text{nodes}} \tilde{H}_i$$

where J is the element's Jacobian, which remains constant for linear elements. The limiting coefficient C_{WD} is computed as follows:

$$\begin{cases} C_{\text{WD}} = 1 & \text{if} \quad V + \Delta V \geq 0 \\ C_{\text{WD}} = 0 & \text{if} \quad V \leq 0 \\ C_{\text{WD}} = \dfrac{V}{|\Delta V|} & \text{otherwise} \end{cases}$$

During the second step, we use the limiting coefficient to compute the flux for each edge and apply the limiter based on the flux direction per edge. Finally, we ensure that the predicted future state maintains $H > H_{\text{thin}}$ at each vertex. If any vertex height is below H_{thin}, we apply a limiter to redistribute the mass within the triangle. This involves computing the minimum and average height of the next state and adjusting the elevations using a weighted average between the vertices' elevations and the triangle's average height, ensuring $H > H_{\text{thin}}$ at each vertex. An example of the computation of the limiting coefficient C_{WD} is given in Fig. C1.

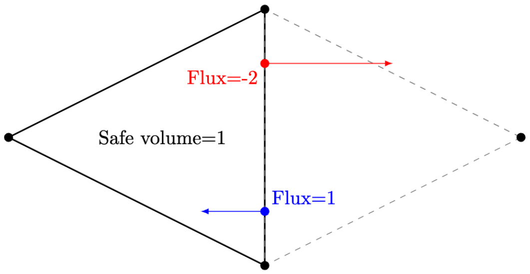

Figure C1. The triangle on the left has a safely removable volume of 1. The total outgoing volume, considering the fluxes at each integration point, is -2. Thus, the limiting coefficient is $C_{\mathrm{WD}} = 1/2$. The next time step volume will be $1 - 2C_{\mathrm{WD}} + 1C_{\mathrm{WD}} = 1/2$.

Author contributions. NRR, MG and EH conzeptualized the study. XF provided the simulation results from the MAR model. NRR performed the model simulation with SLIM, analysis and wrote the initial draft of the paper. JL and MDLC implemented the Wetting and Drying algorithm and provided support with the SLIM model. LA, OG, JL, MG and EH provided inputs and suggestions throughout the project's progression. All authors contributed to reviewing and editing the paper until its final version.

Competing interests. The authors declare that they have no conflict of interest.

Acknowledgements. NRR is a Ph.D. student supported by the Fonds de la Recherche Scientifique de Belgique (F.R.S.-FNRS). LA is a Ph.D. student supported by the Fond pour la formation à la Recherche dans l'Industrie et dans l'Agriculture (FRIA/FNRS). Computational resources have been provided by the supercomputing facilities of the Université catholique de Louvain (CISM/UCLouvain) and the Consortium des Équipements de Calcul Intensif en Fédération Wallonie Bruxelles (CECI/LUCIA) funded by the Fonds de la Recherche Scientifique de Belgique (F.R.S.-FNRS) under convention 2.5020.11.

References

Agulles, M., Marcos, M., Amores, A., and Toomey, T.: Storm Surge Modelling along European Coastlines: The Effect of the Spatio-Temporal Resolution of the Atmospheric Forcing, Ocean Modelling, 192, 102 432, https://doi.org/10.1016/j.ocemod.2024.102432, 2024.

Al Azad, A. S. M. A., Mita, K. S., Zaman, M. W., Akter, M., Asik, T. Z., Haque, A., Hussain, M. A., and Rahman, M. M.: Impact of Tidal Phase on Inundation and Thrust Force Due to Storm Surge, Journal of Marine Science and Engineering, 6, 110, https://doi.org/10.3390/jmse6040110, 2018.

Arndt, S., Lacroix, G., Gypens, N., Regnier, P., and Lancelot, C.: Nutrient Dynamics and Phytoplankton Development along an Estuary–Coastal Zone Continuum: A Model Study, Journal of Marine Systems, 84, 49–66, https://doi.org/10.1016/j.jmarsys.2010.08.005, 2011.

Baptist, M., Babovic, V., Rodríguez Uthurburu, J., Keijzer, M., Uittenbogaard, R., Mynett, A., and Verwey, A.: On Inducing Equations for Vegetation Resistance, Journal of Hydraulic Research, 45, 435–450, https://doi.org/10.1080/00221686.2007.9521778, 2007.

Bart De Maerschalck, Breugem, W. A., Kolokythas, G., and Wang, L.: Scaldis Coast: Numerical Modelling of 10 Years for Long-Term Morphology in the Surf Zone of the Belgian Coast Using the TELEMAC-MASCARET System, in: Proceedings of the XXIXth TELEMAC Users Conference, pp. 108–115, Bundesanstalt für Wasserbau, Karlsruhe, https://doi.org/20.500.11970/112827, 2023.

Bechtold, P., Bazile, E., Guichard, F., Mascart, P., and Richard, E.: A Mass-flux Convection Scheme for Regional and Global Models, Quarterly Journal of the Royal Meteorological Society, 127, 869–886, https://doi.org/10.1002/qj.49712757309, 2001.

Bierly, G.: Extratropical Cyclones, in: Encyclopedia of World Climatology, edited by Oliver, J. E., pp. 373–377, Springer Netherlands, Dordrecht, ISBN 978-1-4020-3266-0, https://doi.org/10.1007/1-4020-3266-8_80, 2005.

Bouwer, L. M.: Have Disaster Losses Increased Due to Anthropogenic Climate Change?, Bulletin of the American Meteorological Society, 92, 39–46, https://doi.org/10.1175/2010BAMS3092.1, 2011.

Brasseur, O.: Development and Application of a Physical Approach to Estimating Wind Gusts, Monthly Weather Review, 129, 5–25, https://doi.org/10.1175/1520-0493(2001)129<0005:DAAOAP>2.0.CO;2, 2001.

Brasseur, O., Ntezimana, V., Gallee, H., d'astronomie et de geophysique Schayes, G. I., and Tricot, C.: Importance of the Convective Adjustment Scheme in the Simulation of the Diurnal Cycle of Convective Activity in Africa, Proceedings of the international conference. Tropical climatology, meteorology and hydrology, pp. 299–312, 1998.

Chen, F., Li, Z., Ding, K., Sun, Z., and Zhou, H.: Assessment and Integration of ERA5 Reanalysis and Fujita-Takahashi Models for Storm Surge Prediction in the East China Sea, Applied Sciences, 13, 10 658, https://doi.org/10.3390/app131910658, 2023.

Cosby, A. G., Lebakula, V., Smith, C. N., Wanik, D. W., Bergene, K., Rose, A. N., Swanson, D., and Bloom, D. E.: Accelerating Growth of Human Coastal Populations at the Global and Continent Levels: 2000–2018, Scientific Reports, 14, 22 489, https://doi.org/10.1038/s41598-024-73287-x, 2024.

Curcic, M. and Haus, B. K.: Revised Estimates of Ocean Surface Drag in Strong Winds, Geophysical Research Letters, 47, e2020GL087 647, https://doi.org/10.1029/2020GL087647, 2020.

Dangendorf, S., Müller-Navarra, S., Jensen, J., Schenk, F., Wahl, T., and Weisse, R.: North Sea Storminess from a Novel Storm Surge Record since AD 1843*, Journal of Climate, 27, 3582–3595, https://doi.org/10.1175/JCLI-D-13-00427.1, 2014.

de Brauwere, A., de Brye, B., Blaise, S., and Deleersnijder, E.: Residence Time, Exposure Time and Connectivity in the Scheldt Estuary, Journal of Marine Systems, 84, 85–95, https://doi.org/10.1016/j.jmarsys.2010.10.001, 2011.

de Brye, B., de Brauwere, A., Gourgue, O., Kärnä, T., Lambrechts, J., Comblen, R., and Deleersnijder, E.: A Finite-Element, Multi-Scale Model of the Scheldt Tributaries, River, Estuary and ROFI, Coastal Engineering, 57, 850–863, https://doi.org/10.1016/j.coastaleng.2010.04.001, 2010.

Dinápoli, M. G., Simionato, C. G., and Moreira, D.: Development and Validation of a Storm Surge Forecasting/Hindcasting Modelling System for the Extensive Río de La Plata Estuary and Its Adjacent Continental Shelf, Natural Hazards, 103, 2231–2259, https://doi.org/10.1007/s11069-020-04079-5, 2020.

Donelan, M. A., Haus, B. K., Reul, N., Plant, W. J., Stiassnie, M., Graber, H. C., Brown, O. B., and Saltzman, E. S.: On the Limiting Aerodynamic Roughness of the Ocean in Very Strong Winds, Geophysical Research Letters, 31, https://doi.org/10.1029/2004GL019460, 2004.

Draoui, I., Lambrechts, J., Legat, V., and Deleersnijder, E.: The Discontinuous Galerkin Method for River-Delta Continuum by Means of a Coupled 1D-2D Shallow Water Model, River Flow 2022, pp. 137–145, https://doi.org/10.1201/9781003323037-19, 2024.

Egbert, G. D., Bennett, A. F., and Foreman, M. G. G.: TOPEX/POSEIDON Tides Estimated Using a Global Inverse Model, Journal of Geophysical Research: Oceans, 99, 24 821–24 852, https://doi.org/10.1029/94JC01894, 1994.

Fettweis, X., Franco, B., Tedesco, M., van Angelen, J. H., Lenaerts, J. T. M., van den Broeke, M. R., and Gallée, H.: Estimating the Greenland Ice Sheet Surface Mass Balance Contribution to Future Sea Level Rise Using the Regional Atmospheric Climate Model MAR, The Cryosphere, 7, 469–489, https://doi.org/10.5194/tc-7-469-2013, 2013.

Fettweis, X., Box, J. E., Agosta, C., Amory, C., Kittel, C., Lang, C., van As, D., Machguth, H., and Gallée, H.: Reconstructions of the 1900–2015 Greenland Ice Sheet Surface Mass Balance Using the Regional Climate MAR Model, The Cryosphere, 11, 1015–1033, https://doi.org/10.5194/tc-11-1015-2017, 2017.

Flather, R. A.: Results from Surge Prediction Model of the North-West European Continental Shelf for April, November and December 1973, Institute of Oceanography (UK), Report, 24, 1976.

Flikweert, J., Cranston, M., Woolhouse, C., Peeters, P., Vonk, B., Müller, J.-M., and Sørensen, P.: Mandela, Sinterklaas, Xaver, Bodil: Impacts and Lessons from the December 2013 Storm Around the North Sea, in: Coastal Management, pp. 555–564, ICE Publishing, Amsterdam, The Netherlands, ISBN 978-0-7277-6114-9, https://doi.org/10.1680/cm.61149.555, 2016.

Gallée, H. and Schayes, G.: Development of a Three-Dimensional Meso-γ Primitive Equation Model: Katabatic Winds Simulation in the Area of Terra Nova Bay, Antarctica, Monthly Weather Review, 122, 671–685, 1994.

Garzon, J. L. and Ferreira, C. M.: Storm Surge Modeling in Large Estuaries: Sensitivity Analyses to Parameters and Physical Processes in the Chesapeake Bay, Journal of Marine Science and Engineering, 4, 45, https://doi.org/10.3390/jmse4030045, 2016.

Geuzaine, C. and Remacle, J.-F.: GMSH: A 3-D Finite Element Mesh Generator with Built-in Pre- and Post-Processing Facilities, International Journal for Numerical Methods in Engineering, 79, 1309–1331, https://doi.org/10.1002/nme.2579, 2009.

Gourgue, O., Comblen, R., Lambrechts, J., Kärnä, T., Legat, V., and Deleersnijder, E.: A Flux-Limiting Wetting–Drying Method for Finite-Element Shallow-Water Models, with Application to the Scheldt Estuary, Advances in Water Resources, 32, 1726–1739, https://doi.org/10.1016/j.advwatres.2009.09.005, 2009.

Gourgue, O., Baeyens, W., Chen, M. S., de Brauwere, A., de Brye, B., Deleersnijder, E., Elskens, M., and Legat, V.: A Depth-Averaged Two-Dimensional Sediment Transport Model for Environmental Studies in the Scheldt Estuary and Tidal River Network, Journal of Marine Systems, 128, 27–39, https://doi.org/10.1016/j.jmarsys.2013.03.014, 2013.

Grailet, J.-F., Hogan, R. J., Ghilain, N., Fettweis, X., and Grégoire, M.: Inclusion of the ECMWF ecRad Radiation Scheme (v1.5.0) in the MAR Model (v3.14), Regional Evaluation for Belgium and Assessment of Surface Shortwave Spectral Fluxes at Uccle Observatory, EGUsphere [preprint], https://doi.org/10.5194/egusphere-2024-1858, 2024.

Hersbach, H., Bell, B., Berrisford, P., Hirahara, S., Horányi, A., Muñoz-Sabater, J., Nicolas, J., Peubey, C., Radu, R., Schepers, D., Simmons, A., Soci, C., Abdalla, S., Abellan, X., Balsamo, G., Bechtold, P., Biavati, G., Bidlot, J., Bonavita, M., De Chiara, G., Dahlgren, P., Dee, D., Diamantakis, M., Dragani, R., Flemming, J., Forbes, R., Fuentes, M., Geer, A., Haimberger, L., Healy, S., Hogan, R. J., Hólm, E., Janisková, M., Keeley, S., Laloyaux, P., Lopez, P., Lupu, C., Radnoti, G., de Rosnay, P., Rozum, I., Vamborg, F., Villaume, S., and Thépaut, J.-N.: The ERA5 Global Reanalysis, Quarterly Journal of the Royal Meteorological Society, 146, 1999–2049, https://doi.org/10.1002/qj.3803, 2020.

Holthuijsen, L. H., Powell, M. D., and Pietrzak, J. D.: Wind and Waves in Extreme Hurricanes, Journal of Geophysical Research: Oceans, 117, https://doi.org/10.1029/2012JC007983, 2012.

Hu, K., Chen, Q., and Wang, H.: A Numerical Study of Vegetation Impact on Reducing Storm Surge by Wetlands in a Semi-Enclosed Estuary, Coastal Engineering, 95, 66–76, https://doi.org/10.1016/j.coastaleng.2014.09.008, 2015.

Ivanov, E., Capet, A., Barth, A., Delhez, E. J., Soetaert, K., and Grégoire, M.: Hydrodynamic Variability in the Southern Bight of the North Sea in Response to Typical Atmospheric and Tidal Regimes. Benefit of Using a High Resolution Model, Ocean Modelling, 154, 101 682, https://doi.org/10.1016/j.ocemod.2020.101682, 2020.

Kärnä, T., de Brye, B., Gourgue, O., Lambrechts, J., Comblen, R., Legat, V., and Deleersnijder, E.: A Fully Implicit Wetting–Drying Method for DG-FEM Shallow Water Models, with an Application to the Scheldt Estuary, Computer Methods in Applied Mechanics and Engineering, 200, 509–524, https://doi.org/10.1016/j.cma.2010.07.001, 2011.

Kerr, P. C., Donahue, A. S., Westerink, J. J., Luettich Jr., R. A., Zheng, L. Y., Weisberg, R. H., Huang, Y., Wang, H. V., Teng, Y., Forrest, D. R., Roland, A., Haase, A. T., Kramer, A. W., Taylor, A. A., Rhome, J. R., Feyen, J. C., Signell, R. P., Hanson, J. L., Hope, M. E., Estes, R. M., Dominguez, R. A., Dunbar, R. P., Semeraro, L. N., Westerink, H. J., Kennedy, A. B., Smith, J. M., Powell, M. D., Cardone, V. J., and Cox, A. T.: U.S. IOOS Coastal and Ocean Modeling Testbed: Inter-model Evaluation of Tides, Waves, and Hurricane Surge in the Gulf of Mexico, Journal of Geophysical Research: Oceans, 118, 5129–5172, https://doi.org/10.1002/jgrc.20376, 2013.

Kjerfve, B., Miranda, L. B., and Wolanski, E.: Modelling Water Circulation in an Estuary and Intertidal Salt Marsh System, Netherlands Journal of Sea Research, 28, 141–147, https://doi.org/10.1016/0077-7579(91)90013-Q, 1991.

Kolokythas, G., De Maerschalck, B., Wang, L, Fonias, S., Breugem, A, Vanlede, J, and Mostaert, F: Modelling Belgian Coastal Zone and Scheldt Mouth Area, Tech. Rep. 12, Flanders Hydraulics Research: Antwerp, 2021.

Lambrechts, J., Comblen, R., Legat, V., Geuzaine, C., and Remacle, J.-F.: Multiscale Mesh Generation on the Sphere, Ocean Dynamics, 58, 461–473, https://doi.org/10.1007/s10236-008-0148-3, 2008.

Le, H.-A., Lambrechts, J., Ortleb, S., Gratiot, N., Deleersnijder, E., and Soares-Frazão, S.: An Implicit Wetting–Drying Algorithm for the Discontinuous Galerkin Method: Application to the Tonle Sap, Mekong River Basin, Environmental Fluid Mechanics, 20, 923–951, https://doi.org/10.1007/s10652-019-09732-7, 2020.

Lewis, H. W., Siddorn, J., Castillo Sanchez, J. M., Petch, J., Edwards, J. M., and Smyth, T.: Evaluating the Impact of Atmospheric Forcing and Air–Sea Coupling on near-Coastal Regional Ocean Prediction, Ocean Science, 15, 761–778, https://doi.org/10.5194/os-15-761-2019, 2019.

Marchesiello, P., McWilliams, J., and Shchepetkin, A.: Open Boundary Conditions for Long-Term Integration of Regional Oceanic Models, Ocean Modelling, 3, 1–20, https://doi.org/10.1016/S1463-5003(00)00013-5, 2001.

Marcos, M., Rohmer, J., Vousdoukas, M. I., Mentaschi, L., Le Cozannet, G., and Amores, A.: Increased Extreme Coastal Water Levels Due to the Combined Action of Storm Surges and Wind Waves, Geophysical Research Letters, 46, 4356–4364, https://doi.org/10.1029/2019GL082599, 2019.

Mathers, E. L. and Woodworth, P. L.: A Study of Departures from the Inverse-Barometer Response of Sea Level to Air-Pressure Forcing at a Period of 5 Days, Quarterly Journal of the Royal Meteorological Society, 130, 725–738, https://doi.org/10.1256/qj.03.46, 2004.

Meire, P., Ysebaert, T., Ysebaert, T., Van Damme, S., Van Damme, S., Van den Bergh, E., Van den Bergh, E., Van den Bergh, E., Maris, T., Eric Struyf, and Struyf, E.: The Scheldt Estuary: A Description of a Changing Ecosystem, Hydrobiologia, 540, 1–11, https://doi.org/10.1007/s10750-005-0896-8, 2005.

Meyer, E. M. I. and Gaslikova, L.: Investigation of Historical Severe Storms and Storm Tides in the German Bight with Century Reanalysis Data, Natural Hazards and Earth System Sciences, 24, 481–499, https://doi.org/10.5194/egusphere-2023-2068, 2023.

Muller, H., Pineau-Guillou, L., Idier, D., and Ardhuin, F.: Atmospheric Storm Surge Modeling Methodology along the French (Atlantic and English Channel) Coast, Ocean Dynamics, 64, 1671–1692, https://doi.org/10.1007/s10236-014-0771-0, 2014.

Nicholls, R. J.: Natural Disaster Hotspots Case Studies, The World Bank Hazard Management Unit, 6, 79–108, 2006.

Patil, A. R., Perez, F. F., Lambrechts, J., Draoui, I., and Deleersnijder, E.: A Multiscale 1D-2D Coupled Model Of The Scheldt Estuary Rivers And The European Continental Shelf, CoastLab 2024: Physical Modelling in Coastal Engineering and Science, https://doi.org/10.59490/coastlab.2024.692, 2024.

Plancke, Y., Stark, J., Meire, D., and Schrijver, M.: Complex Flow Patterns in the Scheldt Estuary: Field Measurements and Validation of a Hydrodynamic Model, Journal of Hydraulic Engineering, 146, 05020 004, https://doi.org/10.1061/(ASCE)HY.1943-7900.0001737, 2020.

Powell, M. D., Vickery, P. J., and Reinhold, T. A.: Reduced Drag Coefficient for High Wind Speeds in Tropical Cyclones, Nature, 422, 279–283, https://doi.org/10.1038/nature01481, 2003.

Pugh, D. T.: Tides, Surges and Mean Sea Level, Wiley, Chichester, ISBN 978-0-471-91505-8, 1987.

Resio, D. T. and Westerink, J. J.: Modeling the Physics of Storm Surges, Physics Today, 61, 33–38, https://doi.org/10.1063/1.2982120, 2008.

Ridder, K. D. and Gallée, H.: Land Surface–Induced Regional Climate Change in Southern Israel, Journal of Applied Meteorology and Climatology, pp. 1470–1485, 1998.

Ridder, N., de Vries, H., Drijfhout, S., van den Brink, H., van Meijgaard, E., and de Vries, H.: Extreme Storm Surge Modelling in the North Sea, Ocean Dynamics, 68, 255–272, https://doi.org/10.1007/s10236-018-1133-0, 2018.

Rodrigues, M., Oliveira, A., Queiroga, H., Brotas, V., and Fortunato, A. B.: Modelling the Effects of Climate Change in Estuarine Ecosystems with Coupled Hydrodynamic and Biogeochemical Models, Developments in Environmental Modelling, 27, 271–288, https://doi.org/10.1016/B978-0-444-63536-5.00012-0, 2015.

Saint-Amand, A., Lambrechts, J., Thomas, C. J., and Hanert, E.: How Fine Is Fine Enough? Effect of Mesh Resolution on Hydrodynamic Simulations in Coral Reef Environments, Ocean Modelling, 186, 102 254, https://doi.org/10.1016/j.ocemod.2023.102254, 2023.

Sampurno, J., Vallaeys, V., Ardianto, R., and Hanert, E.: Modeling Interactions between Tides, Storm Surges, and River Discharges in the Kapuas River Delta, Biogeosciences, 19, 2741–2757, https://doi.org/10.5194/bg-19-2741-2022, 2022.

Schepers, L., Maris, T., Meire, P., and Temmerman, S.: The Scheldt Estuary: An Overview of the Morphodynamics of Intertidal Areas, in: Landscapes and Landforms of Belgium and Luxembourg, edited by Demoulin, A., World Geomorphological Landscapes, pp. 281–296, Springer International Publishing, Cham, ISBN 978-3-319-58239-9, https://doi.org/10.1007/978-3-319-58239-9_17, 2018.

Shu, Y., Wang, D., Zhu, J., and Peng, S.: The 4-D Structure of Upwelling and Pearl River Plume in the Northern South China Sea during Summer 2008 Revealed by a Data Assimilation Model, Ocean Modelling, 36, 228–241, https://doi.org/10.1016/j.ocemod.2011.01.002, 2011.

Smagorinsky, J.: General Circulation Experiments with the Primitive Equations: I. The Basic Experiment, Monthly Weather Review, 91, 99–164, https://doi.org/10.1175/1520-0493(1963)091<0099:GCEWTP>2.3.CO;2, 1963.

Smolders, S., Plancke, Y., Ides, S., Meire, P., and Temmerman, S.: Role of Intertidal Wetlands for Tidal and Storm Tide Attenuation along a Confined Estuary: A Model Study, Natural Hazards and Earth System Sciences, 15, 1659–1675, https://doi.org/10.5194/nhess-15-1659-2015, 2015.

Stark, J., Smolders, S., Meire, P., and Temmerman, S.: Impact of Intertidal Area Characteristics on Estuarine Tidal Hydrodynamics: A Modelling Study for the Scheldt Estuary, Estuarine, Coastal and Shelf Science, 198, 138–155, https://doi.org/10.1016/j.ecss.2017.09.004, 2017.

Statham, P. J.: Nutrients in Estuaries — An Overview and the Potential Impacts of Climate Change, Science of The Total Environment, 434, 213–227, https://doi.org/10.1016/j.scitotenv.2011.09.088, 2012.

Sündermann, J. and Pohlmann, T.: A brief analysis of North Sea physics, Oceanologia, 53, 663–689, https://doi.org/10.5697/oc.53-3.663, 2011.

Taylor, K. E.: Summarizing Multiple Aspects of Model Performance in a Single Diagram, Journal of Geophysical Research: Atmospheres, 106, 7183–7192, https://doi.org/10.1029/2000JD900719, 2001.

Thomas, A., Dietrich, JC., Asher, TG., Bell, M., Blanton, BO., Copeland, JH., Cox, AT., Dawson, CN., Fleming, JG., and Luettich, RA.: Influence of Storm Timing and Forward Speed on Tides and Storm Surge during Hurricane Matthew, Ocean Modelling, 137, 1–19, https://doi.org/10.1016/j.ocemod.2019.03.004, 2019.

Vallaeys, V., Kärnä, T., Delandmeter, P., Lambrechts, J., Baptista, A. M., Deleersnijder, E., and Hanert, E.: Discontinuous Galerkin Modeling of the Columbia River's Coupled Estuary-Plume Dynamics, Ocean Modelling, 124, 111–124, https://doi.org/10.1016/j.ocemod.2018.02.004, 2018.

Vallaeys, V., Lambrechts, J., Delandmeter, P., Pätsch, J., Spitzy, A., Hanert, E., and Deleersnijder, E.: Understanding the Circulation in the Deep, Micro-Tidal and Strongly Stratified Congo River Estuary, Ocean Modelling, 167, 101 890, https://doi.org/10.1016/j.ocemod.2021.101890, 2021.

Van Damme, S., Struyf, E., Maris, T., Ysebaert, T., Dehairs, F., Tackx, M., Heip, C., and Meire, P.: Spatial and Temporal Patterns of Water Quality along the Estuarine Salinity Gradient of the Scheldt Estuary (Belgium and The Netherlands): Results of an Integrated Monitoring Approach, Hydrobiologia, 540, 29–45, https://doi.org/10.1007/s10750-004-7102-2, 2005.

Vanderborght, J.-P., Folmer, I. M., Aguilera, D. R., Uhrenholdt, T., and Regnier, P.: Reactive-Transport Modelling of C, N, and O2 in a River–Estuarine–Coastal Zone System: Application to the Scheldt Estuary, Marine Chemistry, 106, 92–110, https://doi.org/10.1016/j.marchem.2006.06.006, 2007.

Verri, G., Barletta, I., Pinardi, N., Federico, I., Alessandri, J., and Coppini, G.: Shelf Slope, Estuarine Dynamics and River Plumes in a Z* Vertical Coordinate, Unstructured Grid Model, Ocean Modelling, 184, 102 235, https://doi.org/10.1016/j.ocemod.2023.102235, 2023.

Wamsley, T. V., Cialone, M. A., Smith, J. M., Atkinson, J. H., and Rosati, J. D.: The Potential of Wetlands in Reducing Storm Surge, Ocean Engineering, 37, 59–68, https://doi.org/10.1016/j.oceaneng.2009.07.018, 2010.

Ward, N. D., Megonigal, J. P., Bond-Lamberty, B., Bailey, V. L., Butman, D., Canuel, E. A., Diefenderfer, H., Ganju, N. K., Goñi, M. A., Graham, E. B., Hopkinson, C. S., Khangaonkar, T., Langley, J. A., McDowell, N. G., Myers-Pigg, A. N., Neumann, R. B., Osburn,

C. L., Price, R. M., Rowland, J., Sengupta, A., Simard, M., Thornton, P. E., Tzortziou, M., Vargas, R., Weisenhorn, P. B., and Windham-Myers, L.: Representing the Function and Sensitivity of Coastal Interfaces in Earth System Models, Nature Communications, 11, 2458, https://doi.org/10.1038/s41467-020-16236-2, 2020.

Weisse, R., von Storch, H., Niemeyer, H. D., and Knaack, H.: Changing North Sea Storm Surge Climate: An Increasing Hazard?, Ocean & Coastal Management, 68, 58–68, https://doi.org/10.1016/j.ocecoaman.2011.09.005, 2012.

Wetz, M. S. and Yoskowitz, D. W.: An 'Extreme' Future for Estuaries? Effects of Extreme Climatic Events on Estuarine Water Quality and Ecology, Marine Pollution Bulletin, 69, 7–18, https://doi.org/10.1016/j.marpolbul.2013.01.020, 2013.

Woth, K., Weisse, R., and von Storch, H.: Climate Change and North Sea Storm Surge Extremes: An Ensemble Study of Storm Surge Extremes Expected in a Changed Climate Projected by Four Different Regional Climate Models, Ocean Dynamics, 56, 3–15, https://doi.org/10.1007/s10236-005-0024-3, 2006.

Wyard, C., Scholzen, C., Fettweis, X., Van Campenhout, J., and François, L.: Decrease in Climatic Conditions Favouring Floods in the South-East of Belgium over 1959–2010 Using the Regional Climate Model MAR, International Journal of Climatology, 37, 2782–2796, https://doi.org/10.1002/joc.4879, 2017.

Yang, Z., Wang, T., Castrucci, L., and Miller, I.: Modeling Assessment of Storm Surge in the Salish Sea, Estuarine, Coastal and Shelf Science, 238, 106 552, https://doi.org/10.1016/j.ecss.2019.106552, 2020.